

Universidade de São Paulo  
Instituto de Astronomia, Geofísica e Ciências Atmosféricas  
Departamento de Geofísica

# **Mantle Anisotropy and Asthenospheric Flow Around Cratons in SE South America**

Bruna Chagas de Melo  
Supervisor: Marcelo Assumpção

Submitted in partial fulfillment of the requirements for the degree of  
Masters of Science in Geophysics of the University of São Paulo,  
March 2018



## Abstract

Seismic anisotropy at continental regions, mainly at stable areas, gives important information about past and present tectonic events, and helps us in understanding patterns of upper mantle flow in a way not achieved by other methods. The measurement of shear wave splitting (SWS), at individual stations, from core refracted phases (such as SKS phases), indicates the amount and orientation of the seismic anisotropy in the upper mantle. Previous studies of SWS in South America concentrated mainly along the Andes and in southeast Brazil. Now we add extra measurements extending to all Brazilian territory, especially in the Pantanal and Paraná-Chaco basins, as part of the FAPESP “3-Basins Thematic Project”. The results from both temporary deployments and from the Brazilian permanent network provide a more complete and robust anisotropy map of the South America stable platform. In general the fast polarization orientations have an average E-W orientation. Significant deviations to ESE-WNW or ENE-WSW are observed in many regions. We compare our results with different anisotropy proxies: absolute plate motion given by the hotspot reference frame HS3-NUVEL-1A, a recent model of time dependent upper mantle flow induced by the Nazca plate subduction, global anisotropy from surface wave tomography, and geologic trends. We observe a poor correlation of the anisotropy directions with geological trends, with the exception of a few stations in northern Brazil and a better correlation with the mantle flow model. Therefore, our observed anisotropy is mainly due to upper-mantle flow, with little contribution from frozen lithospheric anisotropy. Also, deviations from the mantle flow model, which includes a thicker lithosphere at the Amazon craton, are mainly due to flow surrounding cratonic nuclei not used in the model: the keel of the São Francisco craton and a possible cratonic nucleus beneath the northern part of the Paraná Basin (called Paranapanema block). Large delay times at the Pantanal Basin may indicate a stronger asthenospheric channel, a more coherent flow, or a thicker asthenosphere. Small delays beneath the northern Paraná Basin and central Amazon craton may indicate thinner anisotropic asthenosphere.

**Keywords:** Seismic Anisotropy; Shear Wave Splitting; Mantle Flow; South America.

## Resumo

Anisotropia sísmica em regiões continentais, principalmente em áreas estáveis, nos dá informações importantes sobre eventos tectônicos do passado e do presente, e nos ajuda a entender padrões de fluxo do manto superior de forma não alcançada por outros métodos geofísicos. A medida de separação de ondas cisalhantes (SWS), em estações individuais, de fases refratadas no núcleo (fases SKS, por exemplo), indica a intensidade e orientação da anisotropia sísmica no manto superior. Estudos prévios de SWS na América do Sul se concentraram principalmente ao longo dos Andes e no sudeste do Brasil. Agora adicionamos medidas extras que se estendem por todo território Brasileiro e alguns países vizinhos, especialmente nas bacias do Pantanal e do Chaco-Paraná, como parte do "Projeto Temático 3-Bacias" da FAPESP. Os resultados tanto das estações temporárias quanto da rede permanente Brasileira mostram um mapa de anisotropia mais robusto e completo da plataforma estável da América do Sul. Em geral, as direções de polarização rápida tem em média direção L-O. Desvios significantes nas direções LSL-ONO ou LNL-OSO são observadas em muitas regiões. Comparamos nossos resultados com diferentes representantes da anisotropia: movimento absoluto de placa dado pelo sistema de referência de hotspot HS3-NUVEL-1A, um modelo recente dependente do tempo de fluxo do manto superior induzido pela subducção da placa de Nazca, anisotropia global de tomografia de ondas de superfície, e tendências geológicas. Observamos pouca correlação das direções de anisotropia com tendências geológicas, com exceção de algumas estações no norte do Brasil e uma melhor correlação com o modelo de fluxo do manto. Portanto, nossa anisotropia observada é devida principalmente a fluxo do manto superior, com pouca contribuição de anisotropia "congelada" litosférica. Também, desvios do modelo de fluxo do manto, o qual inclui uma litosfera mais espessa no cráton da Amazônia, são devido ao fluxo ao redor de núcleos cratônicos não usados no modelo: a quilha do cráton do São Francisco e um possível núcleo cratônico abaixo da região norte da bacia do Paraná (chamado bloco do Paranapanema). Atrasos de tempo grandes na bacia do Pantanal podem indicar um canal astenosférico mais forte, um fluxo mais coerente ou uma astenosfera mais espessa. Pequenos atrasos abaixo da parte norte da bacia do Paraná e no centro do cráton da Amazônia podem indicar uma astenosfera mais fina.

**Palavras Chave:** Anisotropia Sísmica; Divisão de Onda Cisalhante; Fluxo do Manto; América do Sul.

# Contents

<b>Abstract</b>	<b>i</b>
<b>Resumo</b>	<b>ii</b>
<b>1 Introduction</b>	<b>1</b>
1.1 Thesis Organization . . . . .	1
1.2 Overview of Project . . . . .	2
1.3 Seismic Anisotropy in the Upper Mantle . . . . .	2
1.4 Shear Wave Splitting . . . . .	4
1.5 Transverse Component Minimization Method . . . . .	6
1.5.1 Two Layer Anisotropy . . . . .	9
<b>2 Paper</b>	<b>16</b>
<b>3 Additional Results and Discussion</b>	<b>65</b>
3.1 Comparison with Different Anisotropy Proxies . . . . .	67
3.2 Two Layer Anisotropy . . . . .	69
<b>4 Conclusion</b>	<b>73</b>
4.1 Final Conclusions . . . . .	73
4.2 Summary of Achievements . . . . .	74
4.3 Future Work . . . . .	74
<b>A Supplementary Material</b>	<b>76</b>
A.1 Figures . . . . .	77



# List of Figures

1.1	Illustration of the creation of olivine LPO at mid-ocean ridges. The a-axis of the olivine crystals tends to align with the lineation direction, in the foliation plane. Therefore, with the flow directions perpendicular to the ridge direction, maximum P- and S-wave seismic velocities are observed in the spreading directions parallel to the a-axis, and minimum velocities in the ridge direction. . . . .	3
1.2	An olivine crystal showing the different seismic velocities on each direction. The a-axis is equivalent to [100] direction, where both P and S velocities are higher compared to the [010] and [001] directions (b and c axes). Figure modified from Stein and Wysession (2002). . . . .	3
1.3	Representation of a shear wave passing through an anisotropic medium. The alignment of anisotropic minerals, as olivine, will cause the waves to split, with the fast component aligned to olivine foliation plane, and a time difference relative to the thickness and intensity of the anisotropic layer. . . . .	5
1.4	Ray paths of a shear wave and a core refracted shear wave. When the teleseismic core refracted shear wave (SKS in this case) crosses the CMB it removes all source side anisotropy. When it encounters an anisotropic medium beneath the station, shear wave splitting will occur. . . . .	6
1.5	The transverse component minimization method finds the pair of parameters $\phi$ and $\delta t$ that best removes the energy on the transverse component seismogram. On the first window is shown a typical ellipsoidal XKS wave particle motion that have crossed an anisotropic layer. After application of the method to remove the effect of anisotropy, the corrected particle motion plot is linearized. . . . .	7

- 1.6 The event analyses window of an SKS wave at station ITAB from the BL network.
- a) Normalized radial and transverse seismogram components showing the SKS wave arrival. Purple bars are 50 randomly selected time windows for statistical analyses. b) Particle motion of the original wave showing an ellipsoidal shape. The purple line shows the back-azimuth direction. c) In the energy grid of the splitting parameters, the pair that best minimizes the energy on the transverse component is chosen (blue cross). The black circle is the error estimated with the 95% confidence level method. d) Particle motion after the application of the method becomes linear, in the direction of the back-azimuth. e) Splitting parameters found and their respective errors. . . . . 9
- 1.7 Distribution of splitting parameters with back-azimuth obtained from AQDB station, BL network. When many measurements do not show large variation with back-azimuth, they can be averaged together. . . . . 10
- 1.8 Comparison of a) the two top graphs are the 1-layer fit of the two anisotropy parameters; with b) bottom graphs show the 2-layer fit of the two anisotropy parameters, all at station PTGB, BL network. Because a large number of events are at the back-azimuthal range from  $220^\circ$  to  $250^\circ$ , these measurements have a higher contribution to the fit in both cases. . . . . 11
- 3.1 All SWS fast directions from this study (black bars) and other published results (gray bars). The bar lengths indicate delay time and good/average qualities of SWS are indicated by thick and thin bars. Red bars are surface wave azimuthal anisotropy directions at 300 km depth. Colors indicate S-wave velocity anomalies at 150 km depth from the surface-wave tomography model SL2013Sv. The white arrow indicates the absolute plate motion in the hotspot reference frame HS3-NUVEL1A. Colored contours are boundaries of major provinces. Null bars (purple bars) are plotted at stations where few or no measurements were found. Bold numbers denote lithosphere/asthenosphere depth from S-wave receiver functions. 66

3.2	SWS orientations compared with the main faults mapped at Brazilian territory. Blue ellipses are the areas where the SWS measurements show a general ESE-WNE direction. In few stations there is a indicative of agreement of the SWS orientation with the direction of the fault alignment. AC: Amazon Craton. . . .	67
3.3	Upper mantle flow directions (a) and LPO directions computed from TI axis (b), both at 250 km compared with the observed fast-polarization orientations (black bars) and their respective histograms of the difference between the SWS direction and the model. (c) comparison of the observed SWS fast directions with the predicted SKS, with its respective histogram (Hu, Faccenda, and Liu, 2017) . . . . .	68
3.4	Two-layer anisotropy results at stations PDRB, PTGB, SALB and VBST plotted with back-azimuth. The curves in green are the 10 best fit models relating the 1 layer apparent parameters to the 2-layer parameters, by the method of Silver and Savage (1994). . . . .	70
3.5	Stations where a 2-layer inversion was calculated compared with a) velocity directions and b) LPO from TI axis, both at 250 km depth, and main fault directions in brown. Black bars are anisotropy directions of the lower layer, purple bars are anisotropy directions of the upper layer and green bars are the 1-layer anisotropy directions. AC: Amazon craton; WPS: Western Parana Suture; Pb: Paranapanema block . . . . .	71
A.1	Station names and their respective networks used in this paper. AC: Amazon craton; SFC: São Francisco craton; Pb: Paranapanema Block. . . . .	78



# Chapter 1

## Introduction

### 1.1 Thesis Organization

This M. Sc. dissertation is formatted into four chapters. Chapter One provides the background information for the project, which includes information on seismic velocity anisotropy, shear wave splitting, the shear wave splitting methodology used herein, and a discussion on two layer anisotropy. Chapter Two is a paper submitted to the Journal of Geophysical International and is currently under revision, to be published shortly. This paper covers the main shear wave splitting results and discussion at the southeast part of stable South America. Because Chapter Two is meant to be a self-containing journal article, some information such as Results and Discussion is stated solely in that chapter. Additional work has been done since the manuscript submission, with more stations analyzed in the northern part of Brazil, and these results will be included in Chapter Three. Chapter Four is a conclusion, of the results from Chapter Two plus the additional results of Chapter Three, plus a summary of the achievements and propositions for future work. An Appendix is supplied, with a table of results, and additional figures.

## 1.2 Overview of Project

We present shear wave splitting (SWS) results of the southeast stable area of South America, including the Pantanal, Paraná and Chaco-Paraná basins as part of the FAPESP "3-Basins Thematic Project". We used a new package called SplitRacer, by Reiss and Rumpker (2017) to perform seismic anisotropy measurements using the Transverse Component Minimization method (Silver and Chan, 1991). The results obtained herein complete the anisotropy map of South America in areas not sampled before and make it possible to better understand our tectonic history and patterns of upper mantle flow. To do so, our measurements are compared to different anisotropy proxies: absolute plate motion given by the hotspot reference frame HS3-NUVEL-1A, upper mantle flow induced by the Nazca plate subduction (Hu, Faccenda, and Liu, 2017), global anisotropy from surface wave tomography (Debayle, Dubuffet, and Durand, 2016) and geologic trends.

## 1.3 Seismic Anisotropy in the Upper Mantle

Seismic anisotropy is the dependence of elastic wave velocity on propagation direction and polarization orientation. One of the most common causes of anisotropy in the mantle is preferred alignment of crystals such as olivine (the most common mineral in the upper mantle) to create lattice preferred orientation (LPO) (Ismail and Mainprice, 1998).

LPO textures are created when crystals within a polycrystalline aggregate are preferentially aligned by an externally imposed deformation mechanism (e.g. Figure 1.1) (Li, Di Leo, and Ribe, 2014). Dislocation creep is commonly presumed to be the dominant mechanism for LPO fabric (Long and Silver, 2009; **Savage1999SeismicSplitting**), although additional deformation mechanisms such as grain boundary sliding, dislocation glide, and diffusion creep may also play a role in causing upper mantle anisotropy (Li, Di Leo, and Ribe, 2014).

In an anisotropic medium with LPO, a seismic wave will travel faster parallel to the a-axis of the olivine and slower if it is perpendicular to that axis (Figure 1.2). Since olivine is one

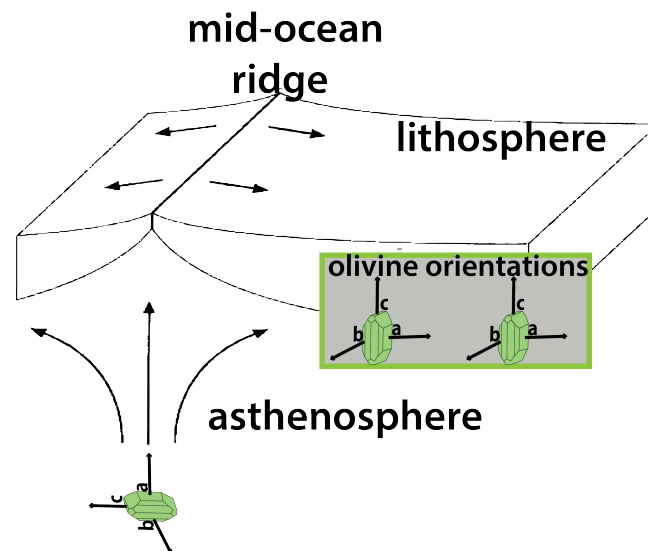


Figure 1.1: Illustration of the creation of olivine LPO at mid-ocean ridges. The *a*-axis of the olivine crystals tends to align with the lineation direction, in the foliation plane. Therefore, with the flow directions perpendicular to the ridge direction, maximum P- and S-wave seismic velocities are observed in the spreading directions parallel to the *a*-axis, and minimum velocities in the ridge direction.

of the main minerals in the upper mantle, and xenolith studies show that for typical mantle conditions it contributes the most to seismic anisotropy (Zhang and Karato, 1995), it is usually assumed that olivine LPO is the primary source of observed anisotropy (Silver and Chan, 1991; Zhang and Karato, 1995; Silver, 1996). LPO can provide information regarding strain and deformation processes in the upper mantle.

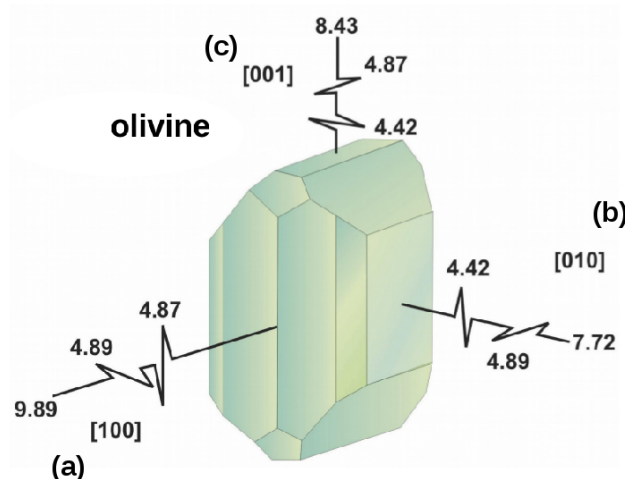


Figure 1.2: An olivine crystal showing the different seismic velocities on each direction. The *a*-axis is equivalent to [100] direction, where both P and S velocities are higher compared to the [010] and [001] directions (*b* and *c* axes). Figure modified from Stein and Wysession (2002).

The observed SWS can be due to anisotropy in the lithospheric mantle (called "frozen" anisotropy), due to past tectonic processes (Silver and Chan, 1991; Silver, 1996), or in the asthenosphere due to present mantle flow (Vinnik et al., 1992). It is now believed that both lithospheric and asthenospheric anisotropies can be present in the same region (Martha Savage, 1999; Silver and Savage, 1994).

Although not studied here, seismic anisotropy can also be observed in other regions within the Earth, such as the transition zone (Karato, 1998), the lower mantle, the D" layer (Kendall and Silver, 1996), and the inner core (Morelli, Dziewonski, and Woodhouse, 1986). Anisotropy in the upper crust can also be formed by the process of shape preferred orientation of cracks (due to stresses) (Crampin, 1987), or preferred mineral alignment in metamorphic fabric (e.g. Nascimento, Bezerra, and Takeya (2004)). The contribution of crustal anisotropy to SKS splitting is usually very small ( $\leq 0.1$  s), and is usually ignored in studies of mantle anisotropy.

## 1.4 Shear Wave Splitting

The most common method to measure the effect of anisotropy is shear wave splitting (SWS). This phenomenon is analogous to optical birefringence and occurs when a seismic shear wave encounters an anisotropic medium (e.g., LPO fabric of olivine) (Martha Savage, 1999). Upon encountering an anisotropic medium, the shear wave is split into two orthogonally polarized waves traveling at different velocities, one faster and one slower, orthogonal wave Figure 1.3 (Silver, 1996; Long and Silver, 2009). The splitting is characterized by two parameters:

$$\phi = \textit{fast orientation} \tag{1.1}$$

$$\delta t = \textit{delay time} \tag{1.2}$$

which refer to the polarization orientation of the first-arriving "fast" split shear wave and the time difference between the two polarized shear waves, respectively. The fast axis orientation

is sensitive to the geometry of the anisotropic fabric and the split time is proportional to the thickness and intensity of the anisotropic layer (Silver and Chan, 1991). A null measurement is one where splitting cannot be detected for one of four reasons: there is no splitting or the polarization of the XKS wave is parallel or perpendicular to the orientation of the olivine foliation plane. A different and more complex type of anisotropy, such as orientations varying with depth, or tilted fast axes of the olivine crystals (Baptiste and Tommasi, 2014).

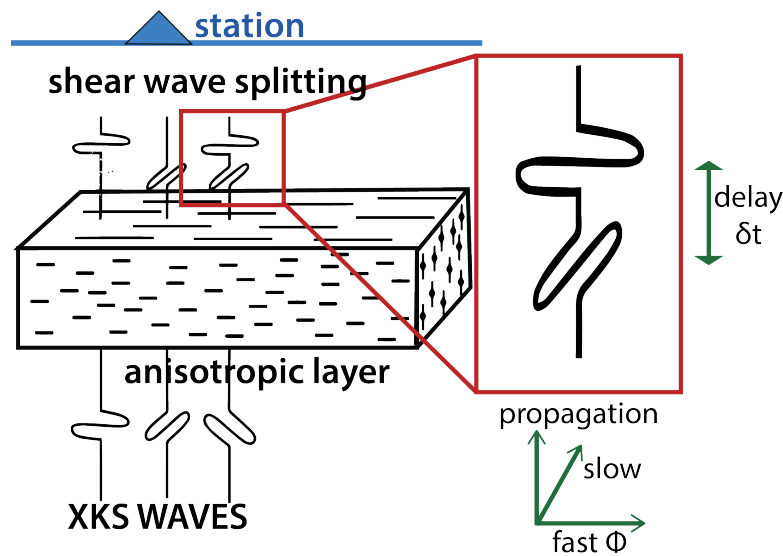


Figure 1.3: Representation of a shear wave passing through an anisotropic medium. The alignment of anisotropic minerals, as olivine, will cause the waves to split, with the fast component aligned to olivine foliation plane, and a time difference relative to the thickness and intensity of the anisotropic layer.

To perform shear wave splitting analysis we use core-refracted seismic wave phases as SKS, SKKS, and PKS (hereafter named as XKS, Figure 1.4). Teleseismic XKS are used in SWS analyses because they are radially polarized when they are converted from a compressional (P) wave to a vertical shear (SV) wave at the core-mantle boundary (CMB). This radial polarization at the CMB removes all source-side effects and therefore, all measured anisotropy comes from the path of the receiver side (Silver and Chan, 1991; Long and Silver, 2009). Moreover, XKS phases travel in a nearly vertical direction through the mantle, which simplifies the analysis but makes it difficult to resolve the depth at which the measured anisotropy is occurring (Long and Silver, 2009).

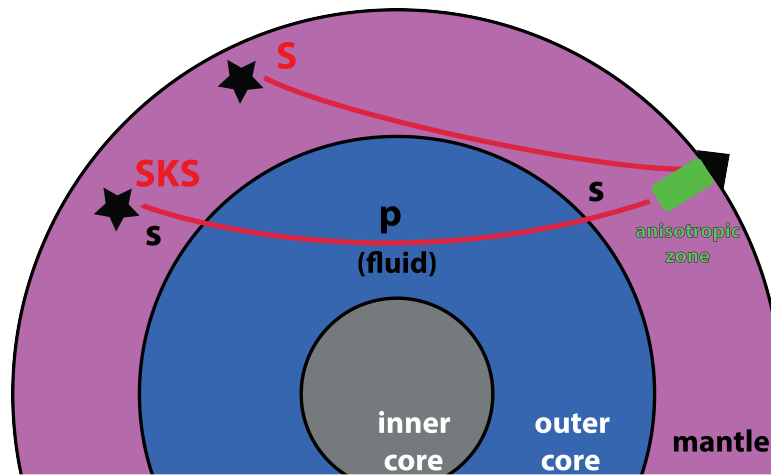


Figure 1.4: Ray paths of a shear wave and a core refracted shear wave. When the teleseismic core refracted shear wave (SKS in this case) crosses the CMB it removes all source side anisotropy. When it encounters an anisotropic medium beneath the station, shear wave splitting will occur.

## 1.5 Transverse Component Minimization Method

Due to conversion from P to SV wave at the CMB, in the absence of an anisotropic layer, the XKS is assumed to arrive at the seismic station with energy only in the radial component. The transverse component minimization method, introduced by Silver and Chan (1991), attempts to reverse the effects of splitting by finding the pair of anisotropy parameters that best minimizes the energy on the transverse component (that is assumed to be propagating in a near vertical direction upwards from the source to the station) using an inverse splitting operator Figure 1.5.

In order to carry out the Silver and Chan (1991) method we require observations of shear waves as inputs. In an isotropic, homogeneous medium a shear wave can be written as a vector function:

$$\mathbf{u}(\omega) = \mathbf{A}(\omega)\exp[-i\omega T_o] \quad (1.3)$$

where, as specified by Walsh, Arnold, and Savage (2013):

$\omega = \text{angular frequency}$

$\mathbf{u}(\omega) = \text{isotropic shear wave vector}$

$\mathbf{A}(\omega) = w(\omega)\hat{\mathbf{A}}(\omega)$  complex amplitude vector

$w(\omega) = \|\mathbf{A}(\omega)\|$  norm of the amplitude with angular frequency  $\omega$

$T_0 = \text{time at which the wave arrives at the surface}$

To represent the propagation coordinates (P), a right handed set of orthogonal vectors  $[\hat{\mathbf{p}}\hat{\mathbf{b}}\hat{\mathbf{a}}]$

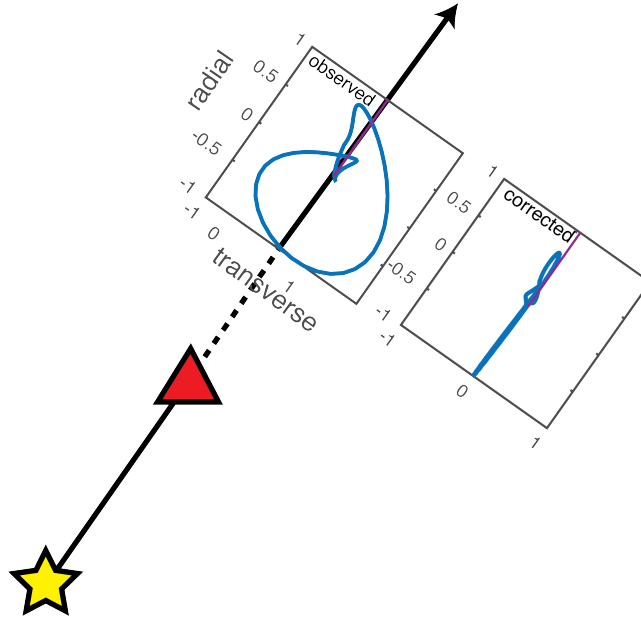


Figure 1.5: The transverse component minimization method finds the pair of parameters  $\phi$  and  $\delta t$  that best removes the energy on the transverse component seismogram. On the first window is shown a typical ellipsoidal XKS wave particle motion that have crossed an anisotropic layer. After application of the method to remove the effect of anisotropy, the corrected particle motion plot is linearized.

are defined. The three orthogonal vectors that define this coordinate system are

$\hat{\mathbf{b}} = \text{propagation vector}$

$\hat{\mathbf{p}} = \text{polarisation vector pointing in the direction of shear wave displacement}$

$$\hat{\mathbf{a}} = \hat{\mathbf{b}} \times \hat{\mathbf{p}}$$

Silver and Chan (1991) assume that waves (for all frequencies  $\omega$ ) displace in the same direction  $\hat{\mathbf{p}}$ . Therefore the complex amplitude vector  $\mathbf{A}(\omega)$  can be approximated by replacing  $\hat{\mathbf{A}}(\omega)$  with  $\hat{\mathbf{p}}$  for all  $\omega$ . Therefore Equation 1.3 is rewritten as:

$$\mathbf{u}(\omega) = w(\omega)\exp[-i\omega T_o]\hat{\mathbf{p}} \quad (1.4)$$

The splitting due to anisotropy is modeled as the geometrical operations of projecting  $\hat{\mathbf{p}}$  onto the fast and slow polarization directions fast  $\hat{\mathbf{f}}$  and slow  $\hat{\mathbf{s}}$ , and then time shift these two components by  $\delta t/2$  (earlier) and  $-\delta t/2$  (later) respectively. The process of producing a split shear wave can be represented as the application of the splitting operator:

$$\Gamma \equiv \exp[i\omega\delta t/2]\hat{\mathbf{f}}\hat{\mathbf{f}} + \exp[-i\omega\delta t/2]\hat{\mathbf{s}}\hat{\mathbf{s}} \quad (1.5)$$

to the wave equation, with the resulting split waveform:

$$\mathbf{u}_s(\omega) = w(\omega)\exp[-i\omega T_o]\Gamma(\phi, \delta t)\hat{\mathbf{p}} \quad (1.6)$$

where  $\phi$  is the angle between  $\hat{\mathbf{f}}$  and  $\hat{\mathbf{p}}$ . Defining the tensor

$$\delta T = \delta t/2(\hat{\mathbf{f}}\hat{\mathbf{f}} - \hat{\mathbf{s}}\hat{\mathbf{s}}) \quad (1.7)$$

$\Gamma$  can be more compactly written as

$$\Gamma = \exp[i\omega\delta T(\phi, \delta t)] \quad (1.8)$$

in analogy with the isotropic case Equation 1.4.

We want to estimate the parameters  $\phi$  and  $\delta t$ . To do so, we perform a grid search over all possible pairs of  $\phi$  and  $\delta t$  and choose the pair that most nearly returns Equation 1.6 into the form Equation 1.4 by reversing the geometrical operations, that is, search for the inverse operator  $\Gamma^{-1}$ . This operator is unitary, therefore the inverse is the complex conjugate  $\Gamma^*$ . The method assumes a single layer of anisotropy and that two of the three symmetry axes lie in the

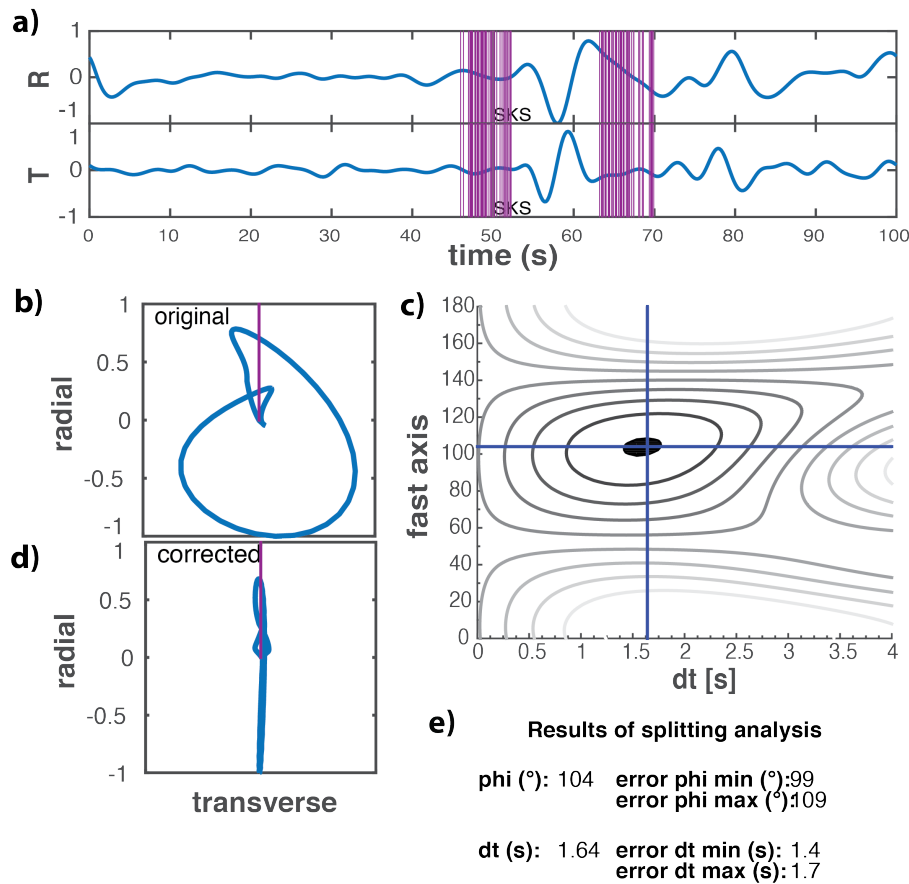


Figure 1.6: The event analyses window of an SKS wave at station ITAB from the BL network. a) Normalized radial and transverse seismogram components showing the SKS wave arrival. Purple bars are 50 randomly selected time windows for statistical analyses. b) Particle motion of the original wave showing an ellipsoidal shape. The purple line shows the back-azimuth direction. c) In the energy grid of the splitting parameters, the pair that best minimizes the energy on the transverse component is chosen (blue cross). The black circle is the error estimated with the 95% confidence level method. d) Particle motion after the application of the method becomes linear, in the direction of the back-azimuth. e) Splitting parameters found and their respective errors.

horizontal plane. Error estimations are made with the 95% confidence test. The application of this method has been made with the aid of the SplitRacer package by (Reiss and Rumpker, 2017). Figure 1.6 shows an example of SWS analyses.

### 1.5.1 Two Layer Anisotropy

When using the Transverse Component Minimization method, it is assumed that there is a single homogeneous layer of anisotropy under the receiver (Silver and Chan, 1991). In this way, the anisotropy parameters  $\phi$  and  $\delta t$  have no variation with incident angle and back-azimuth,

and many measurements can be averaged together, e.g. Figure 1.7.

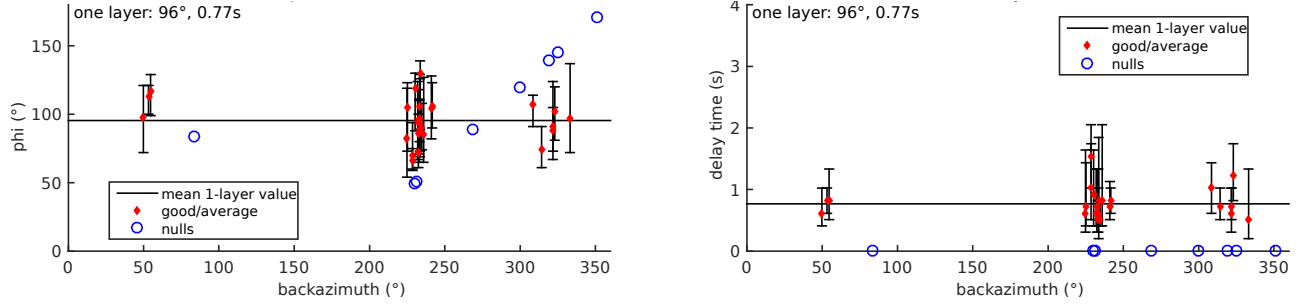


Figure 1.7: Distribution of splitting parameters with back-azimuth obtained from AQDB station, BL network. When many measurements do not show large variation with back-azimuth, they can be averaged together.

However, in some cases these assumptions do not represent the reality, and the parameters may have a dependence with back-azimuth. For example, dipping symmetry will have  $2\pi$  periodicity with back-azimuth, and if two anisotropic layers are present, the splitting parameters will have a  $\pi/2$  periodicity with back-azimuth. Silver and Savage (1994) have shown that the splitting parameters obtained assuming a one layer anisotropy (here referred as apparent splitting parameters) are still meaningful, and that there are simple trigonometric functions to relate them to the 2-layer parameters  $\phi_1$ ,  $\delta t_1$ ,  $\phi_2$  and  $\delta t_2$ . Silver and Savage (1994) define the parameters:  $\alpha_{1,2} = 2\phi_{1,2}$ , where  $\phi_{1,2}$  is the angle between the initial polarization (back-azimuth)  $\phi_p$  and the fast polarization orientation of the layer (1,2), and  $\theta_{1,2} = \omega\delta t_{1,2}/2$ . Now they define  $a_p$ ,  $a_{p\perp}$ ,  $C_c$  e  $C_s$  by:

$$a_p = \cos\theta_1\cos\theta_2 - \sin\theta_1\sin\theta_2\cos(\alpha_2 - \alpha_1) \quad (1.9)$$

$$a_{p\perp} = -\sin\theta_1\sin\theta_2\sin(\alpha_2 - \alpha_1) \quad (1.10)$$

$$C_c = \cos\theta_1\sin\theta_2\cos\alpha_2 + \cos\theta_2\sin\theta_1\cos\alpha_1 \quad (1.11)$$

$$C_s = \cos\theta_1\sin\theta_2\sin\alpha_2 + \cos\theta_2\sin\theta_1\sin\alpha_1 \quad (1.12)$$

and express the apparent splitting parameters  $\phi_a$  e  $\delta t_a$  as:

$$\tan\phi_a = \frac{a_{p\perp}^2 + C_s^2}{a_{p\perp}a_p + C_sC_c} \quad (1.13)$$

$$\tan\delta t_a = \frac{a_{p\perp}}{C_s\cos\alpha_a - C_c\sin\alpha_a} = \frac{C_s}{a_p\sin\alpha_a - a_{p\perp}\cos\alpha_a} \quad (1.14)$$

$$(1.15)$$

This group of equations provide the direct method of using the 2-layer parameters to find the 1 layer apparent parameters. The SplitRacer (Reiss and Rumpker, 2017) package used in this work to calculate the 1 layer anisotropy parameters also provides the tools to perform the inversion and to find the best fit of the 2-layer anisotropy parameters based on this method of Silver and Savage (1994) (Figure 1.8).

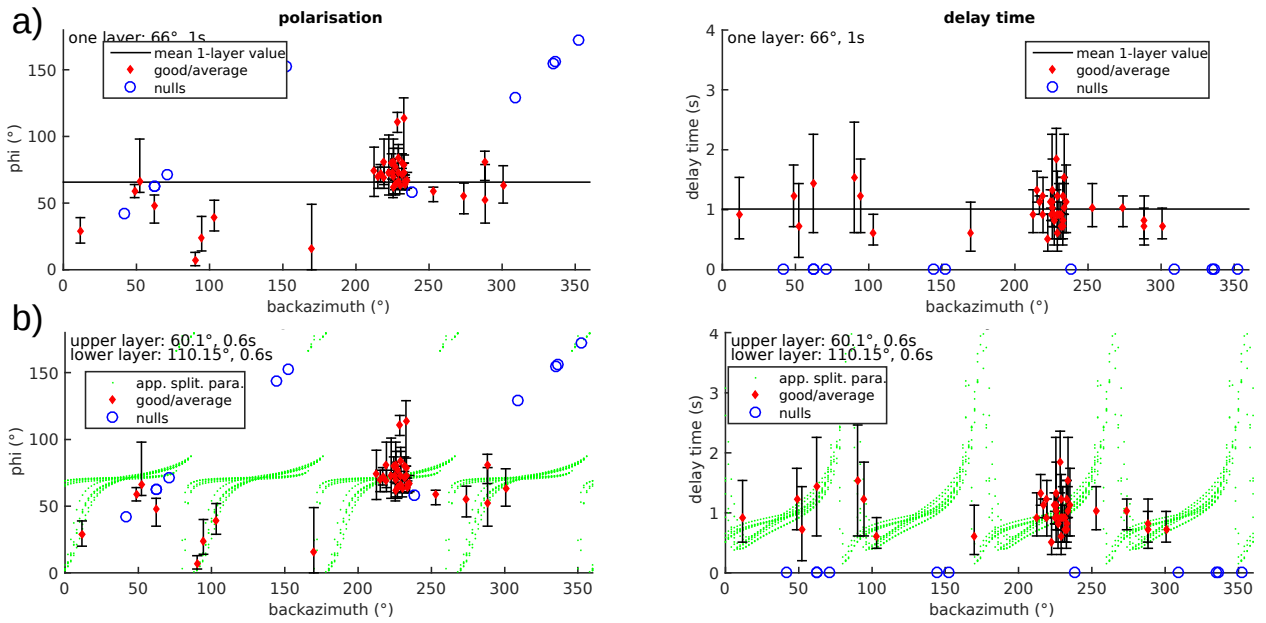


Figure 1.8: Comparison of a) the two top graphs are the 1-layer fit of the two anisotropy parameters; with b) bottom graphs show the 2-layer fit of the two anisotropy parameters, all at station PTGB, BL network. Because a large number of events are at the back-azimuthal range from  $220^\circ$  to  $250^\circ$ , these measurements have a higher contribution to the fit in both cases.

There are many situations where more than one layer is present, and in a stable continental region, it is common to exist both fossil anisotropy in the lithosphere, as well as anisotropy associated with upper mantle flow in the asthenosphere (Silver and Chan, 1991; Silver and Savage, 1994).

Among the stations analyzed in this study there are many that exhibit signs of a more complex form of anisotropy in the form of disperse measurements that can not be well fitted by one single value of  $\phi$  and  $\delta t$  (such as station PTGB in Figure 1.8). Some attempts have been made to find a 2-layer anisotropy case, and they will be discussed in Chapter 3. For most cases, due to poor back-azimuthal distribution of the events, a clear 2-layer case could not be identified and a single layer of anisotropy fitted the data well.

# Bibliography

- Baptiste, V. and A. Tommasi (2014). “Petrophysical constraints on the seismic properties of the Kaapvaal craton mantle root”. In: *Solid Earth*. ISSN: 18699510. DOI: 10.5194/se-5-45-2014.
- Crampin, S. (1987). “Geological and industrial implications of extensive-dilatancy anisotropy”. In: *Nature*. ISSN: 0028-0836. DOI: 10.1038/328491a0.
- Debayle, E., F. Dubuffet, and S. Durand (2016). “An automatically updated S-wave model of the upper mantle and the depth extent of azimuthal anisotropy”. In: *Geophysical Research Letters*. ISSN: 19448007. DOI: 10.1002/2015GL067329.
- Hu, J., M. Faccenda, and L. Liu (2017). “Subduction-controlled mantle flow and seismic anisotropy in South America”. In: *Earth and Planetary Science Letters*. ISSN: 0012821X. DOI: 10.1016/j.epsl.2017.04.027.
- Ismail, W. B. and D. Mainprice (1998). “An olivine fabric database: An overview of upper mantle fabrics and seismic anisotropy”. In: *Tectonophysics*. ISSN: 00401951. DOI: 10.1016/S0040-1951(98)00141-3.
- Karato, S. (1998). “Seismic Anisotropy in the Deep Mantle, Boundary Layers and the Geometry of Mantle Convection”. In: *Pure and Applied Geophysics*. ISSN: 0033-4553. DOI: 10.1007/s000240050130.
- Kendall, J.-M. and P. G. Silver (1996). “Constraints from seismic anisotropy on the nature of the lowermost mantle”. In: *Nature* 381, p. 409. URL: <http://dx.doi.org/10.1038/381409a0>.
- Li, Z.-H., J. F. Di Leo, and N. M. Ribe (2014). “Subduction-induced mantle flow, finite strain, and seismic anisotropy: Numerical modeling”. In: *Journal of Geophysical Research: Solid*

- Earth* 119.6, pp. 5052–5076. ISSN: 21699313. DOI: 10.1002/2014JB010996. URL: <http://doi.wiley.com/10.1002/2014JB010996>.
- Long, M. D. and P. G. Silver (2009). *Shear wave splitting and mantle anisotropy: Measurements, interpretations, and new directions*. DOI: 10.1007/s10712-009-9075-1.
- Martha Savage (1999). “Seismic anisotropy and mantle deformation: What have we learned from shear wave splitting?” In: *Reviews of Geophysics*. DOI: 10.1029/98RG02075.
- Morelli, A., A. M. Dziewonski, and J. H. Woodhouse (1986). “Anisotropy of the inner core inferred from PKIKP travel times”. In: *Geophysical Research Letters* 13.13, pp. 1545–1548. DOI: 10.1029/GL013i013p01545. URL: <http://doi.wiley.com/10.1029/GL013i013p01545>.
- Nascimento, A. F. do, F. H. Bezerra, and M. K. Takeya (2004). “Ductile Precambrian fabric control of seismic anisotropy in the Aç u dam area, northeastern Brazil”. In: *Journal of Geophysical Research B: Solid Earth*. ISSN: 01480227. DOI: 10.1029/2004JB003120.
- Reiss, M. C. and G. Rumpker (2017). “SplitRacer: MATLAB Code and GUI for Semiautomated Analysis and Interpretation of Teleseismic Shear-Wave Splitting”. In: *Seismological Research Letters*. ISSN: 0895-0695. DOI: 10.1785/0220160191.
- Silver, P. G. (1996). “Seismic Anisotropy Beneath the Continents: Probing the Depths of Geology”. In: *Annual Review of Earth and Planetary Sciences*. DOI: 10.1146/annurev.earth.24.1.385.
- Silver, P. G. and W. W. Chan (1991). “Shear wave splitting and subcontinental mantle deformation”. In: *Journal of Geophysical Research*. ISSN: 0148-0227. DOI: 10.1029/91JB00899.
- Silver, P. G. and M. K. Savage (1994). “The Interpretation of Shear Wave Splitting Parameters In the Presence of Two Anisotropic Layers”. In: *Geophysical Journal International*. DOI: 10.1111/j.1365-246X.1994.tb04027.x.
- Stein and Wysession (2002). *An Introduction to Seismology, Earthquakes and Earth Structure-Wiley (2002)*. John Wiley and Sons.
- Vinnik, L. P. et al. (1992). “Global patterns of azimuthal anisotropy and deformations in the continental mantle”. In: *Geophys. I. Znt* 111, pp. 433–447.
- Walsh, E., R. Arnold, and M. K. Savage (2013). “Silver and Chan revisited”. In: *Journal of Geophysical Research: Solid Earth*. ISSN: 21699356. DOI: 10.1002/jgrb.50386.

---

Zhang, S. and S. Karato (1995). "Lattice preferred orientation of olivine aggregates deformed in simple shear". In: *Nature*. DOI: 10.1038/375774a0.

# Chapter 2

## Paper

This chapter consists of a manuscript submitted to the Journal of Geophysical International on the 17th of October of 2017. On December 22nd, 2017, moderate revision was asked by the Editor following recommendations of two reviewers. Accordingly, this manuscript version contains all modifications asked by the reviewers, with some additional maps and information. All changes to the original manuscript are highlighted in blue and the side notes explain which alterations were made.

# Mantle Anisotropy and Asthenospheric Flow Around Cratons in Southeastern South America

Bruna Chagas de Melo, Marcelo Assumpção, and the "3-Basins" Project Team

*Centro de Sismologia, Departamento de Geofísica, Instituto de Geofísica, Astronomia, e Ciências Atmosféricas, Universidade de São Paulo, São Paulo, Brazil.*

---

## Abstract

Upper mantle seismic anisotropy is one of the most important means to study dynamics of the Earth's interior. It has been extensively used to infer past and present mantle dynamics and continental evolution. Seismic anisotropy in the upper mantle can be measured by the method of shear wave splitting (SWS) of core refracted phases, such as SKS. Previous studies of SWS in South America concentrated mainly along the Andes and in southeast Brazil. Now we add extra measurements in the area of the Pantanal and Chaco-Paraná basins, as part of the FAPESP "3-Basins" thematic project. With the splitting results of 47 new stations, we have a more complete and robust anisotropy map of the South America stable platform. On average, over most of the mid plate continent, the fast polarizations have an average E-W orientation, which is close to the absolute plate motion given by the hotspot reference model HS3-NUVEL-1A (median deviation of  $15.7^\circ$ ). However, recent models of subduction induced mantle flow beneath South America provide a better explanation for the fast orientations (median deviation of  $\approx 12^\circ$ ). Nevertheless, detailed analyses of the fast orientations indicate an additional component of mantle flow deviating from the cratonic blocks, at the São Francisco and Amazon cratons, and beneath the Paraná basin (called Paranapanema block). Large delay times may indicate a strong asthenospheric channel, a more coherent flow, or a thicker asthenosphere, between the Paranapanema block and the Amazon craton. Similarly, small delay times may indicate thinner anisotropic asthenosphere beneath the Paranapanema block.

*Keywords:* Anisotropy, Shear Wave Splitting, Asthenospheric Flow

---

1 **1. Introduction**

2 The study of seismic anisotropy beneath continents, particularly in stable  
3 areas, yields important constraints on past and present tectonic processes,  
4 and helps understanding patterns of sub-lithospheric mantle flow, in a way  
5 that cannot be achieved by other geophysical methods. Shear wave split-  
6 ting is now a standard method for studying seismic anisotropy in the upper  
7 mantle, consisting of local measurements at individual stations. The result-  
8 ing splitting parameters are usually interpreted as due to preferred mineral  
9 alignment, which could reflect mantle flow directions related to present-day  
10 plate motions and/or "fossil" deformation preserved in the lithospheric man-  
11 tle since the last major <sup>c1</sup>tectonic event<sup>c2</sup>.

c1 orogeny

12 Seismic anisotropy is the dependence of wave speed on the direction  
13 of seismic polarization and wave propagation. A shear wave propagating  
14 through an anisotropic medium is split into two orthogonal quasi-shear waves,  
15 one traveling faster than the other (Silver, 1996). The polarization orienta-  
16 tion of the fast component is usually named fast polarization orientation ( $\phi$ )  
17 of anisotropy. The two waves travel at different speeds; therefore, a delay  
18 time ( $\delta t$ ) is observed between the "fast" and "slow" components when they  
19 arrive at the station. The amount of delay time depends on the thickness of  
20 the anisotropic layer and/or the strength of anisotropy. When there is a delay  
21 time between the fast and slow components of core refracted phases, such as  
22 SKS, SKKS and PKS phases (here nominated XKS), they will exhibit some  
23 energy on the tangential component producing an elliptical particle motion.  
24 Analyses of the fast polarization orientation ( $\phi$ ) and delay time ( $\delta t$ ) provide  
25 simple measurements that characterize seismic anisotropy directly beneath  
26 the receiving seismic station.

c2 changed orogeny  
to tectonic event as  
requested by  
reviewer 1

27 Fast polarization directions measured by shear wave splitting (SWS) are  
28 related to lattice preferred orientation (LPO) of anisotropic minerals (es-  
29 pecially olivine), caused by shear deformation in the mantle (Silver, 1996).  
30 Studies of mantle xenoliths show that anisotropy can be as high as 7 % (Ismail  
31 and Mainprice, 1998). Deformation through dislocation creep (crystalline  
32 dislocations within grains) is needed to cause preferred mineral orientation,  
33 and it occurs with high stress, large grain size, or both (Savage, 1999).

34 <sup>c3</sup> Some authors such as Silver and Chan (1991) and Silver (1996) argued  
35 that the fast polarization orientation in stable continents correlate better with

c3 The origin of  
seismic anisotropy  
in continental areas  
as measured by  
SWS has been a big  
debate.

36 <sup>c4</sup>crustal structural trends, implying that "frozen" anisotropy imprinted by  
37 past lithospheric deformation is the main source of anisotropy. <sup>c5</sup>It is also  
38 believed that anisotropy is formed by the alignment of fast propagation ori-  
39 entations with current, or geologically recent, mantle flow (Vinnik et al.,  
40 1992; Fouch et al., 2000; Becker et al., 2014). Becker et al. (2014) <sup>c6</sup>explores  
41 two different scenarios: 1) the comparison of azimuthal anisotropy directions  
42 with absolute plate motion (APM) models, under the assumption that the  
43 mantle at some larger depth is relatively stationary, such that surface veloc-  
44 ities are directly related to the asthenosphere, and 2) the comparison with  
45 mantle flow, which he argues to be a plausible, global back-ground model of  
46 azimuthal anisotropy for oceanic plates and their underlying asthenosphere.  
47 <sup>c7</sup>Specially in continental areas, some studies show contribution from litho-  
48 sphere thickness variation, inducing flow around cratonic roots (Fouch et al.,  
49 2000; Assumpção et al., 2006; Becker et al., 2012). <sup>c8</sup>

50 Initial studies in SWS in Southeast Brazil indicated strong correlation of  
51 fast orientations with geological trends (James and Assumpção, 1996; Heintz  
52 et al., 2003). However, later studies in a larger region (Assumpção et al.,  
53 2006);(Assumpção et al., 2011) tended to favor upper mantle flow around  
54 cratonic roots, with fossil anisotropy restricted to few localized areas. Here  
55 we expanded the shear wave splitting measurements further to the west with  
56 newly installed stations (Figure 1) to have a more complete regional pattern.

57 Our results reveal that the São Francisco and Amazon cratons, and an  
58 anomalous high velocity block in the Paraná basin, interpreted as a cratonic  
59 nucleus (Mantovani et al., 2005), modulate the anisotropy orientation by  
60 diverting mantle flow.

## 61 2. Geological Setting

### 62 2.1. Paraná Basin

63 The Paraná basin of southern Brazil (Figure 1 - contour in brown) is  
64 a typical Paleozoic intracratonic basin and hosts one of the largest igneous  
65 provinces of the world <sup>c1</sup>,the Cretaceous Serra Geral Formation<sup>c2</sup> (Milani and  
66 De Wit, 2008). The central and northern parts of the basin have been studied  
67 by passive seismology in the past 20 years, but little is known of the upper  
68 mantle structure in the west of the basin, especially in Paraguay, NE Ar-  
69 gentina, and beneath the Chaco Basin. In some areas, the lithosphere could  
70 be up to 200 km thick, as revealed by the compilation of Steinberger and  
71 Becker (2016). Julià et al. (2008) used receiver function and Rayleigh-wave

<sup>c4</sup> tectonic structures in the crust

<sup>c5</sup> A common interpretation is that shear deformation due to relative motion of the lithosphere with respect to the asthenosphere orients the olivine a-axis and therefore causes the fast directions,  $\phi$  to be oriented parallel to the plate motion. Other models suggest that olivine LPO could be induced by larger-scale flow in the asthenosphere. The fast direction would coincide with the direction of flow but might differ from the direction of plate motion if the plate is decoupled from the flow beneath it.

<sup>c6</sup> Text added.

<sup>c7</sup> Text added.

<sup>c8</sup> This paragraph was changed to add the suggestion of the reviewer 1, which was to add some detail as explored by Becker et al. (2014).

<sup>c1</sup> Text added.

<sup>c2</sup> added the age of the tectonic province as requested by reviewer 2

72 dispersion to confirm that the basin sediments are underlain by a predomi-  
73 nantly cratonic nucleus (Mantovani et al., 2005; Cordani, 1984), and mafic  
74 underplating only occurred under selected sites, possibly channeled between  
75 fragmented cratonic roots as seen in the model of Milani and Ramos (2017).

76 Previous measurements of SWS in this area are scarce (Assumpção et al.,  
77 2011), and show a trend of small delays with a general E-W fast direction,  
78 which has been mainly correlated with the absolute plate motion directions  
79 in the HS3-NUVEL-1A frame (Gripp and Gordon, 2002).

## 80 2.2. Pantanal Basin

81 The Pantanal basin (Figure 1 - Pt) is a shallow ( $\sim 400\text{m}$ ), Quaternary  
82 basin between the deep intracratonic Paraná basin and the sub-Andean  
83 basins (Assine and Soares, 2004). Both regional (Feng et al., 2007) and global  
84 (Schaeffer and Lebedev, 2013) tomography models show a strong S-wave low-  
85 velocity anomaly in the upper mantle (100-300 km depth), concentrated at  
86 the basin and continuing to the NE in the Tocantins Province. Ussami et al.  
87 (1999) proposed that the formation and subsidence of the basin resulted from  
88 extensional flexural stresses due to the Andean load, in a migrating foreland  
89 bulge. However, seismicity in the Pantanal basin is characterized by shal-  
90 low, reverse faulting events (Dias et al., 2016), which makes subsidence due  
91 to flexural extension unlikely. Studies of SWS may help better understand  
92 the upper mantle dynamics in this area and <sup>c1</sup><sup>c2</sup> shed light on the formation  
93 mechanism of this Quaternary Basin.

94 Again, previous measurements (Assumpção et al., 2011) in this area have  
95 poor coverage, due to a lack of stations. Assumpção et al. (2006, 2011)  
96 analyzed stations AQDB and PP1B <sup>c3</sup>(see Fig. S1, at the Supplementary  
97 Material, for station names and locations)<sup>c4</sup>, as they were the only ones in  
98 the area at the time. <sup>c5</sup>The few measurements were compared with flow par-  
99 allel to APM as well with flow <sup>c6</sup> surrounding the positive S-wave anomaly  
100 in the Paraná basin.

<sup>c1</sup> ~~contribute to~~  
<sup>c2</sup> removed  
contribute to as  
suggested by  
reviewer 1

<sup>c3</sup> Text added.

<sup>c4</sup> A supplementary  
figure with all  
station names and  
locations is  
provided at the  
Supplementary  
Material, as  
suggested by  
reviewer 2.

<sup>c5</sup> ~~and have shown a  
deviation from the  
proposed APM  
model~~

<sup>c6</sup> Changed this  
phrase for better  
clarity.

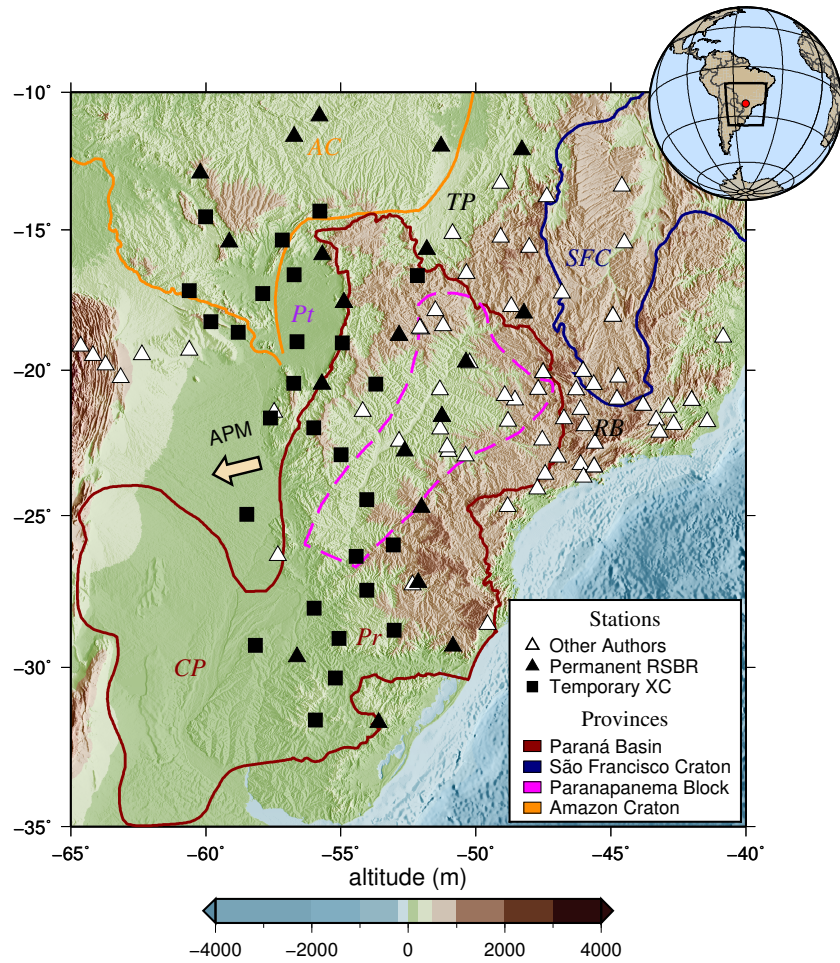


Figure 1: Stations with the new and old measurements of SWS in southeastern South America (shown in black and white fill). The colored contours show the main geological provinces here discussed. Labels on the map are: SFC - São Francisco craton; CP - Chaco-Paraná basin (western part of the basin); Pr - Paraná basin (eastern part of the basin), Pt - Pantanal basin; TP - Tocantins foldbelt province; RB - Ribeira foldbelt; AC - Amazon craton. The yellow arrow is the absolute plate motion direction in the HS3-NUVEL-1A frame.

### 101 3. Data and Method

102 A 3-year experiment (called “3-Basins” experiment, for short) deployed 35  
103 temporary stations, with an average station spacing of 400 km, to study the  
104 crust and upper mantle structure beneath the Pantanal, Paraná and Chaco-  
105 Paraná Basins (Figure 1). Here we show the first SWS results from this  
106 experiment together with data from the permanent Brazilian Seismographic  
107 Network (RSBR) (<sup>c1</sup>see Fig. S1), analyzed between January 2011 and May  
108 2017 <sup>c2</sup>(Tables S1 and S2). We examined core refracted phases (XKS), with  
109 distances  $\geq 85^\circ$  and magnitude  $\geq 5.6$ . For earthquakes deeper than 100 km,  
110 this magnitude is the limit to acceptable signal-to-noise ratio (SNR). Events  
111 with poor SNR ( $< 2$ ) were discarded. Seismograms were bandpass filtered  
112 between 0.03 and 0.3 Hz, with the exception of stations with low SNR and  
113 stations that showed evidences of complex anisotropy, <sup>c3</sup>for which we also ex-  
114 amined the effect of small-scale changes in anisotropy at higher frequencies,  
115 with a bandpass filter from 0.15 to 0.5 Hz.<sup>c4</sup>

116 To determine the two anisotropy parameters: fast-polarization orienta-  
117 tion ( $\phi$ ) and delay time ( $\delta t$ ) we used a Matlab based software: the SplitRacer  
118 package (Reiss and Rumpker, 2017). Shear wave splitting (SWS) is analyzed  
119 based on the <sup>c5</sup>transverse-component energy minimization method of Silver  
120 and Chan (1991). To apply this method, we must know the initial polariza-  
121 tion of the wave, which is always assumed for core-phases to correspond to  
122 the station back-azimuth. <sup>c6</sup>The package also has a misalignment check tool,  
123 <sup>c7</sup>based on the difference between the orientation of the ellipse drawn by the  
124 XKS particle motion and the back-azimuth (<sup>c8</sup>Fig. S2). <sup>c9</sup>After manual se-  
125 lection of the events, we compared the misalignment angles calculated by the  
126 package, based on the XKS particle motions, with misalignment measured  
127 by P-wave particle motions by Bianchi (2015), <sup>c10</sup>and they were equivalent.  
128 When the average value of misalignment was higher than  $10^\circ$ , the correction  
129 was applied.<sup>c11</sup>

130 Figure 2 shows an example of splitting analysis for an event recorded at  
131 station ITAB. The SplitRacer package uses a grid search for the splitting  
132 parameters ( $\phi$ ) and ( $\delta t$ ) carried out to minimize the energy on the transverse  
133 component, after removing the anisotropy effect. This is done within a time  
134 window initially chosen around the phase and is repeated for 50 random  
135 window variations (Figure 2-a,b). The results for each time window are  
136 then plotted in histograms (Figure 2-c), which are used to calculate mean  
137 splitting parameters and to check the consistency of the results. Errors are

<sup>c1</sup> Text added.

<sup>c2</sup> Text added.

<sup>c3</sup> ~~where the bandpass was adapted.~~

<sup>c4</sup> Added specification about how the filter parameters were adapted for complex waveforms, as suggested by reviewer 2.

<sup>c5</sup> Text added.

<sup>c6</sup> ~~After manual selection of the events,~~

<sup>c7</sup> ~~a misalignment check is performed,~~

<sup>c8</sup> Text added.

<sup>c9</sup> ~~The results matched the misalignment measured with P-wave particle motions. A correction was then applied to the misaligned stations.~~

<sup>c10</sup> Text added.

<sup>c11</sup> Added more specifications on the misalignment check performed, and the reference for the p-wave polarization measurements, as suggested by reviewer 2.

138 calculated with 95 % confidence levels from the F-test as in Silver and Chan  
139 (1991) (Figure 2-f,g). Based on clear phase arrivals, particle motion plots,  
140 histogram distribution, error and percentage of transverse energy reduction,  
141 we classify the results as good, average, poor or null.

142 After application of the inverse splitting operator on the XKS phase,  
143 the elliptical particle motion should become linear (Figure 2-e), and the his-  
144 togram should show one clear peak for each parameter. If the anisotropy  
145 correction does not lead to linearization of the particle motion, the event is  
146 classified as poor and not used in the analyses. When the wave arrives at the  
147 anisotropic layer with polarization perpendicular or parallel to the fast-axis  
148 direction, the wave is not split, and thus, arrives without transverse energy.  
149 These measurements are called nulls, and they can also represent complex  
150 anisotropic structures as discussed by Bastow et al. (2015). When there is  
151 a clear phase arrival, but no energy on the transverse component and both  
152 the particle motions from before and after the inversion are linear, the event  
153 is classified as null. In this case, the energy grid shows 95% confidence levels  
154 usually along the whole delay-time axis, at two narrow values of fast orien-  
155 tations, corresponding to the back-azimuth and its perpendicular direction.

156 <sup>c1</sup> <sup>c2</sup>To investigate whether a one layer model of anisotropy is suitable,  
157 single station measurements<sup>c3</sup> are inspected for azimuthal dependency, e.g.  
158 Figure 3-a,b,c. For example, a two-layer case with different anisotropic  
159 properties will have splitting parameters with a  $\frac{\pi}{2}$  periodicity as a func-  
160 tion of back azimuth (Savage, 1999). <sup>c4</sup>However, for stations localized in  
161 South America we have a restricted back-azimuthal coverage of events, which  
162 makes it difficult to observe this periodicity, or other forms of complex  
163 anisotropy.Figure 4<sup>c5</sup> shows the map of event location and the polar his-  
164 tograms of the event azimuthal coverage of some stations at different loca-  
165 tions. The main source of usable events for SWS splitting analysis comes from  
166 the Fiji islands, and covers back-azimuths from 215° to 245°. In fewer cases,  
167 there are events from Alaska (290° to 340°), and from the Mediterranean  
168 (40° to 60°). At some stations (Fig. S20), it seems that the anisotropy is  
169 more complex than a single layer model, and the 2-layer model could fit the  
170 data better. Yet, it has not been observed in this study any case where a two  
171 layers of anisotropy can be considered conclusively. At stations with a larger  
172 variability of the parameters with back-azimuth, a simple mean of all events  
173 was calculated (Table S1.) <sup>c6</sup>At the stations where the one layer model fitted  
174 well the data (Table S2), we applied a joint splitting analysis consisting of  
175 using all waveforms<sup>c7</sup>, and simultaneously minimizing the transverse energy

<sup>c1</sup> We added more information about the back-azimuthal coverage in the text, as well as a figure showing some examples of back-azimuthal distribution. We also added the graphs of the anisotropy parameters versus back-azimuth of all stations at the Supplementary Data.

<sup>c2</sup> Single

<sup>c3</sup> ~~at one station~~

<sup>c4</sup> ~~If azimuthal variations are not significant, a single layer of anisotropy is assumed.~~

<sup>c5</sup> Text added.

<sup>c6</sup> ~~When this is the case~~

<sup>c7</sup> ~~at a given station~~

176 on all of them, resulting in a more robust pair of splitting parameters (Fig-  
177 ure 3-d,e,f). The corrected transverse components are concatenated so that  
178 the sum of the energy on all transverse components is used in the grid search  
179 for the splitting parameters. This approach significantly reduces the influ-  
180 ence of noise and increases the robustness of the splitting results, avoiding  
181 over-interpretation of single-phase results (Reiss and Rumpker, 2017). The  
182 application of the inverse splitting parameters should lead to a linearization  
183 of the particle motions of all waveforms, and then a single layer of anisotropy  
184 explains the observations.<sup>c8</sup>

185

c1

~~c8 Nevertheless, it is possible that due to a poor distribution of back-azimuths, a two-layer case or other anisotropic complexities exist, but are not detected.~~

c1 Changed the blue color at the pie chart of Figure 3 to red, to facilitate the visualization of the labels, as suggested by reviewer 2.

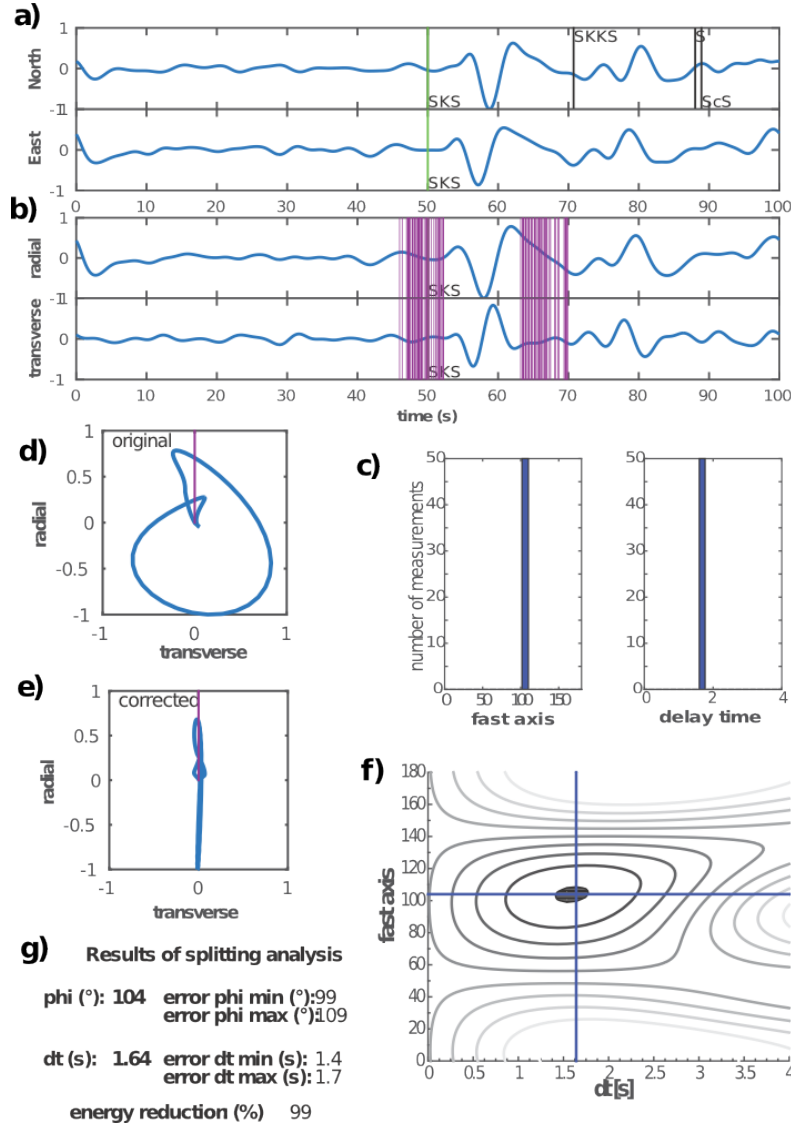


Figure 2: Analysis of an SKS phase at the station ITAB from the RSBR network. a) Normalized original North and East components. b) Normalized radial and transverse components. The purple lines are 50 randomly selected time windows. c) Histograms of fast axis ( $\phi$ ) and delay time results from the 50 different time windows. d) Original particle motion. The purple bar is the back-azimuth. e) Particle motion after correction. f) Energy grid of the corrected transverse component. The black contour level refers to the 95 % confidence level. The blue cross marks the pair of splitting parameters which best minimizes the energy on the transverse component. g) Results of the splitting parameters with errors, and the energy reduction rate.

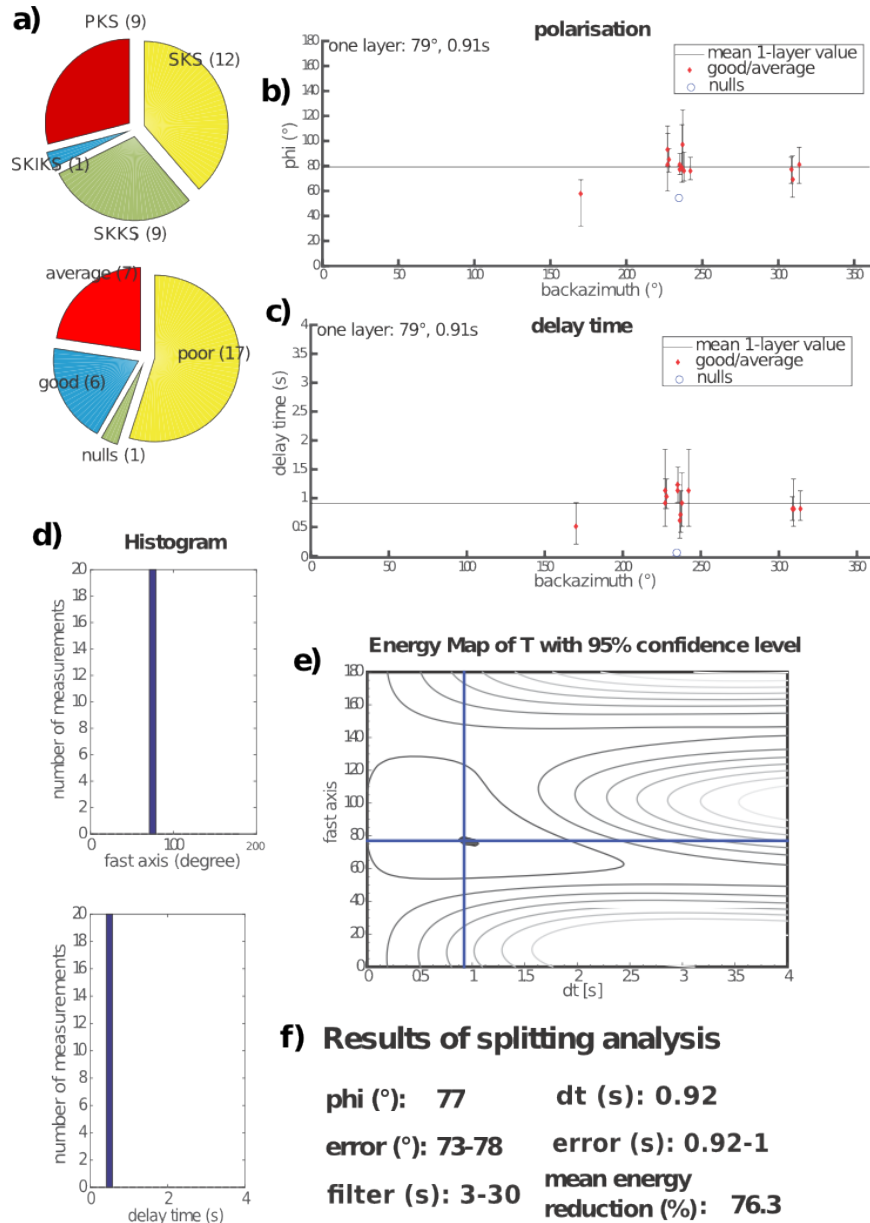


Figure 3: Compilation of the events analyzed at station PP1B. a) Pie charts showing distribution of phases used and classification of the events. b) Polarization of fast-direction measurements plotted against back-azimuth. The black line represents the mean value, written at the top of the graph. c) Delay times and their respective back-azimuths. d) Histogram of the joint-inversion of all events of this station. e) Energy map of the joint-inversion. f) Results given by the joint-inversion.

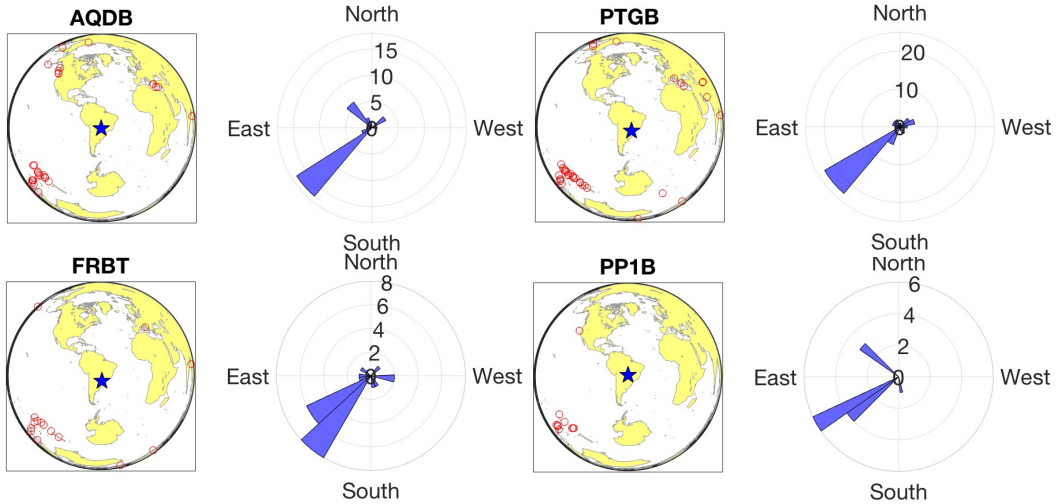


Figure 4: Maps of event distribution per station. The blue star is the location of the station and the red circles are the events used in the SWS analyses. The respective polar histograms are the back-azimuthal coverage of events at stations AQDB, FRBT, PP1B, SALV

#### 186 4. Results and Discussion

187 The 45 new SWS measurements from both temporary and permanent  
 188 stations are presented in Figure 5 <sup>c1</sup>(Table S1 and S2), together with pre-  
 189 vious compilations for the stable part of South America (Assumpção et al.,  
 190 2006)assumpcao2011. The gap in XKS measurements between the Andes  
 191 and SE Brazil is now partly filled, and we provide a more complete and ro-  
 192 bust anisotropy map of the South America stable platform. A general trend  
 193 can be recognized, where most fast orientations tend to be oriented E-W,  
 194 roughly parallel to the absolute plate motion in the hot-spot reference frame  
 195 HS3-NUVEL1A (Gripp and Gordon (2002)). However, regional variations  
 196 can be observed: ESE-WNW orientations and small delays just south of the  
 197 Amazon craton, large delays and mostly ENE-WSW orientations in the Pan-  
 198 tanal basin, small delays and E-W fast orientations in the northern part of  
 199 the Paraná Basin, and ESE-WNW in the southern part of the Paraná basin.

##### 200 4.1. Comparison with Surface Wave Azimuthal Global Anisotropy

201 <sup>c2</sup> <sup>c3</sup>Shear wave splitting measurements have excellent lateral resolution,  
 202 but no resolution with depth. Here we investigate the origin of upper mantle  
 203 anisotropy by comparison with the surface wave azimuthal global anisotropy

<sup>c1</sup> Text added.

<sup>c2</sup> We add global surface wave anisotropy directions at Figure 5, and a section to discuss this comparison as suggested by reviewer 1.

<sup>c3</sup> Text added.

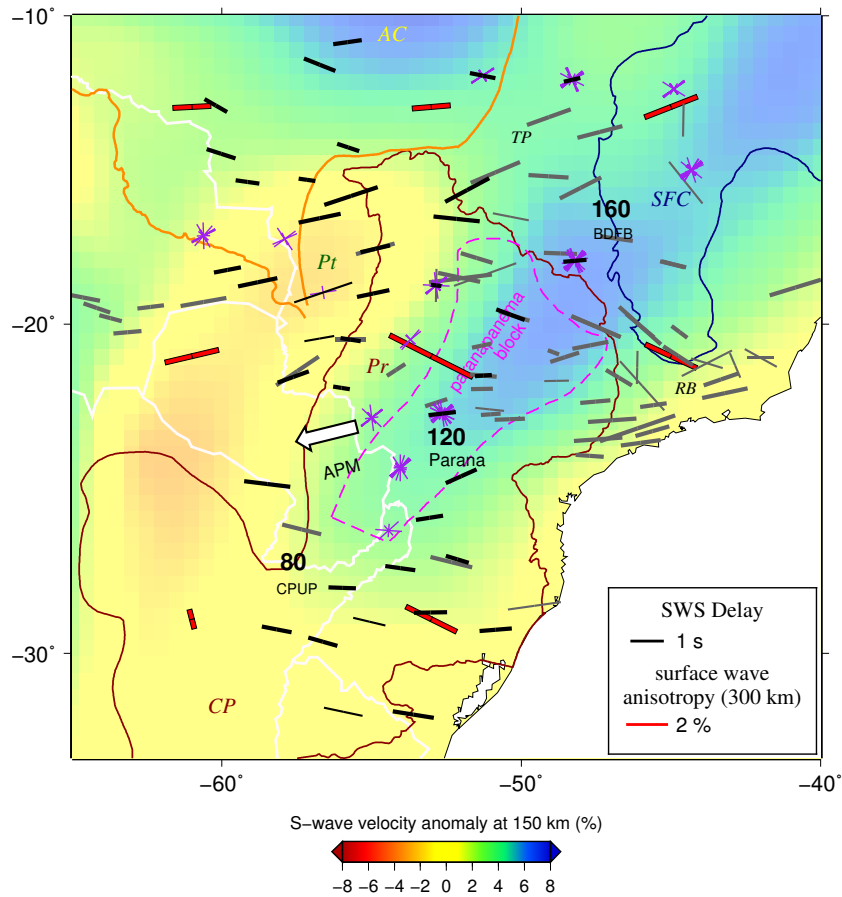


Figure 5: SWS fast directions from this paper are black bars and other published results (gray bars). The bar lengths indicate delay time and good (5 or events events used) /average qualities of SWS are indicated by thick and thin bars. Red bars are surface wave azimuthal anisotropy directions at 300 km depth from Debayle et al. (2016). Colors indicate S-wave velocity anomalies at 150 km depth from the surface-wave tomography model SL2013 (Schaeffer and Lebedev, 2013). The white arrow indicate the absolute plate motion in the hotspot reference frame HS3-NUVEL1A (Gripp and Gordon, 2002). Colored contours are the major provinces boundaries. Null bars (as purple bars) are plotted at stations where few or no measurements were found. Bold numbers denote lithosphere/asthenosphere depth from S-wave receiver functions Heit et al. (2007).

204 directions from the model of Debayle et al. (2016). <sup>c4</sup>A qualitative compar-  
 205 parison has been made at different upper mantle depths (Figure S22), and  
 206 we observed that the SWS anisotropy directions correlate better with the  
 207 surface wave anisotropy directions at 300 km depth(Figure 5). <sup>c5</sup>Surface wave  
 208 anisotropy from global models have low lateral resolution, therefore the influ-

<sup>c5</sup> Text added.

<sup>c4</sup> Text added.

209 ence of regional lithospheric topography is hardly observed. There is a overall  
210 E-W trend, which match our orientations, specially at the northern Parana  
211 basin, at the Pantanal basin and at the Amazon craton. Moreover, the direc-  
212 tions at the keel of the SFC have the same SW trend. At the southern Chaco-  
213 Parana basin the SWS orientations have a slight ESE rotation, tending to the  
214 NW-SE orientation shown by the surface wave anisotropy directions. The fact  
215 that our measurements correlate better with surface wave anisotropy at 300  
216 km depth, lead us to believe that the main source of anisotropy in SE South  
217 America comes from asthenospheric mantle flow and that the lithospheric,  
218 frozen anisotropy has little to no contribution.

c1

219

#### 220 4.2. Comparison with Geologic Trends

221 <sup>c2</sup> <sup>c3</sup>In Figure 6<sup>c4</sup> we see the main geologic provinces of the study area and  
222 basement fault directions. In addition, a recent study of crustal structure  
223 with gravity and geological data by Dragone et al. (2017)<sup>c5</sup> proposed a N-S  
224 trending suture zone between the Pantanal and Paraná basins from 15°W to  
225 30°W, called Western Paraná Suture (WPS, green contour in ??).

226 <sup>c6</sup>In the Pantanal basin and the northern Paraná basin ??-b <sup>c7</sup>there is  
227 a main ENE-SWS alignment, which correlates with the fault directions at  
228 the most part of the northern Paraná basin, but do not with the basement  
229 fault direction under the Pantanal basin, which is N-S. Also, the WPS has  
230 N-S alignment in this region. In Figure 6-c)<sup>c8</sup> the anisotropy directions have a  
231 general E-W to ESE-WNW directions, in agreement with the direction of the  
232 WPS. However this is inconclusive as the general trend of the entire area is in  
233 the E-W direction. Moreover, there is no correlation with the fold belt direc-  
234 tions under the basin, which are NE. Although effects of frozen anisotropy in  
235 the lithospheric mantle had been suggested in some parts of SE Brazil (James  
236 and Assumpção, 1996; Heintz et al., 2003; Assumpção et al., 2011), we note  
237 the fast polarization orientations do not correlate with the main geological  
238 trends.<sup>c9</sup>

c1 There has been a modification in the order of the items discussed here, to better accommodate the new topics. We now discuss the frozen anisotropy before the comparison with the tomography features, to make clearer the reason why we discard these effects in our interpretation.

c2 We also add a figure of geologic trends, and discuss in more detail the existence of frozen anisotropy, as suggested by reviewer 2.

c3 Text added.

c4 Text added.

c5 Text added.

c6 Text added.

c7 Text added.

c8 Text added.

c9 ~~with the exception of few measurements at the Ribeira belt, south of the Sao Francisco craton (SFC).~~

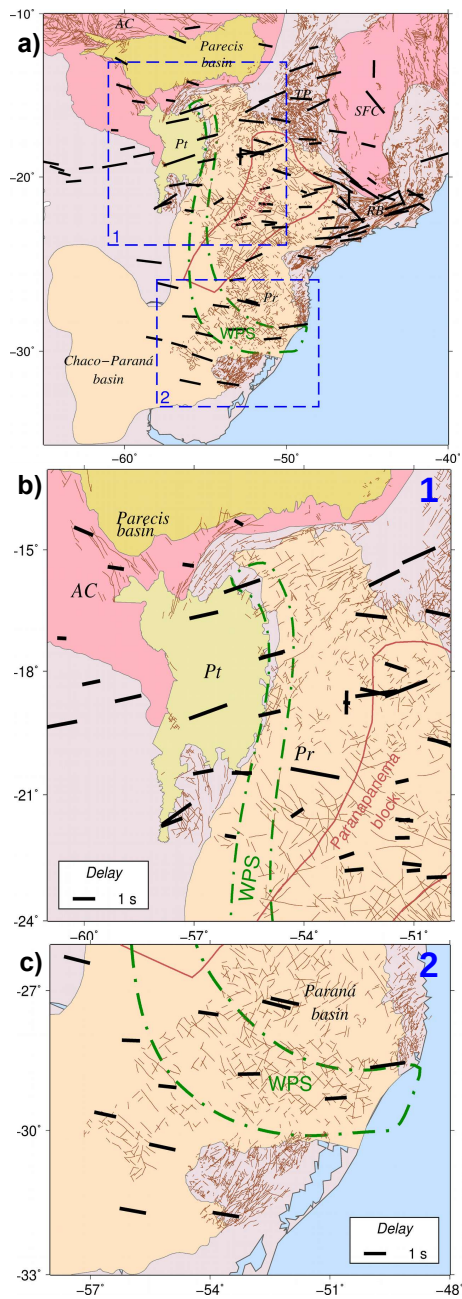


Figure 6: Main geologic provinces in South America. AC: Amazon craton; SFC: São Francisco craton; TP: Tocantins Province; Pt: Pantanal basin; RB: Ribeira Belt; WPS: West Paraná Suture (Dragone et al., 2017). Brown lines are basement faults mapped by CPRM (Brazilian Geological Survey), and the dashed squares are the areas with more measurements selected for comparison of the SWS directions with the fault trends. a) Geology of the study region. The dashed squares 1 and 2 are shown in more detail at b) and c), respectively. b) Mainly the ENE-WSW directions observed at the Pantanal and northern Paraná basin. c) E-W directions observed at the southern Paraná basin.

239 *4.3. Comparison with Lithospheric Depths*

240 We now discuss possible relations between the fast SWS orientation with  
241 a thick lithospheric block beneath the northern part of the Paraná basin.  
242 The positive and negative S-wave anomalies derived from the surface-wave  
243 tomography, shown in Figure 5 (Schaeffer and Lebedev, 2013) are a qual-  
244 itative indication of the depth of the lithosphere. As we wish to check if  
245 variations in the lithospheric thickness are influencing the flow directions in  
246 the asthenosphere, we compare our results with the tomography anomalies  
247 at 150 km depth and with the lithosphere-asthenosphere boundary at a few  
248 stations obtained with S-wave receiver function (Heit et al., 2007). <sup>c1</sup>We  
249 find that the thickest lithosphere (160 km) at station BDFB corresponds to  
250 +5% S-wave anomaly at 150 km depth. The thin part of the lithosphere ( $\leq$   
251 80 km at CPUP) is associated with an S-wave anomaly value of only 1%.  
252 In the Paraná Basin, a stack of 10 temporary stations showed an average  
253 lithosphere-asthenosphere boundary of 120 km depth, which is consistent  
254 with about 4.5% S-wave anomalies. This means that the S-wave velocity  
255 anomaly at 150 km depth can be used as a rough proxy for the lithospheric  
256 thickness. We have three separate main deep lithospheric roots: one at the  
257 southern part of the Amazon craton, one at the São Francisco craton, and one  
258 in the NE part of the Paraná basin. The positive anomaly in the tomogra-  
259 phy in the Paraná basin corresponds roughly to the cratonic block defined by  
260 Cordani (1984), based on radiometric dates and geological evidences. Man-  
261 tovani et al. (2005) used gravity data to delimit this cratonic block, calling it  
262 Paranapanema block (Figure 5-in dashed pink). <sup>c2</sup>Considering that the posi-  
263 tive anomalies correspond to thicker lithospheres, we observe an ENE-WSW  
264 trend of the SWS orientations from the Pantanal basin to the Tocantins  
265 Province, north of the thick lithosphere of the Paranapanema block. Like-  
266 wise, there is an ESE-WNW orientation group south of the Paranapanema  
267 thick lithosphere. Therefore, we consider that <sup>c3</sup>the main contribution to the  
268 fast polarization orientations comes from asthenospheric flow and flow mod-  
269 ulation due to lithosphere thickness variation at cratonic keels, especially  
270 around the SFC (Assumpção et al., 2006), and the Amazon cratons. The  
271 suggested flow surrounding the Paranapanema block in the Paraná basin, as  
272 will be shown below.

273 *4.4. Comparison with Mantle Flow*

274 The SKS splitting observed at the surface is the compound effect of the  
275 passage of the shear wave through a complex series of anisotropic layers in the

<sup>c1</sup> Labels of stations CPUP and BDFB are added to the tomography map at Figure 5, as asked by the editor. Also a map of all stations used is added to the Supplementary Material.

<sup>c2</sup> Text added.

<sup>c3</sup> ~~frozen anisotropy plays a minor role in the observed SWS, and~~

276 upper mantle. Comparing the fast orientation with any single parameter can  
277 be an over-simplification of heterogeneous and complex structure. However,  
278 it is useful to compare the fast orientations with some simple proxies for the  
279 anisotropy effect in an attempt to get insight into the main contribution to  
280 the observed shear wave splitting.

281 In this section we compare our SWS results with three different proxies  
282 of anisotropy: absolute plate motion with respect to the deep mantle (hot  
283 spot reference frame NUVEL1A-HS3), convection velocity <sup>c1</sup>and computed  
284 LPO, with respect to the overriding South American plate from the model  
285 of Hu et al. (2017). <sup>c2</sup>

286 <sup>c3</sup>The model of Hu et al. (2017) calculates <sup>c4</sup>time-dependent upper mantle  
287 flow driven by the evolution of the Nazca plate subduction since the Mid-  
288 Cretaceous. Conrad et al. (2007), Assumpção et al. (2011) and Miller and  
289 Becker (2012) had already compared their results with mantle flow models.  
290 However, these studies only utilized instantaneous mantle flow models. A  
291 time-dependent flow is needed to better predict seismic anisotropy, due to the  
292 long term response of anisotropic minerals to the cumulative strain (Ribe,  
293 1992). This recent convection model depends on the subduction history  
294 and slab geometry and should better represent the real Earth, compared to  
295 models based on tomography images or parameterized slab geometry (Hu  
296 et al., 2017). <sup>c5</sup>To compute the strain-induced LPO directions of the mineral  
297 aggregates, the model calculates transverse isotropy, i.e. TI axis from full  
298 elastic tensors. TI axis of upper mantle aggregates approximately coincides  
299 with the direction of maximum stretching and fastest seismic velocity, and  
300 when sub-horizontal, define the orientation of the XKS wave fast component  
301 and maximum SWS is expected (Faccenda and Capitanio, 2013). <sup>c6</sup>More-  
302 over, it uses the kinematic model D-Rex of Kaminski et al. (2004)<sup>c7</sup> which  
303 includes plastic deformation, dynamic recrystallization and grain boundary  
304 sliding, and incorporates these deformation mechanisms to compute LPO  
305 using the constrained mantle flow history.<sup>c8</sup>

306 <sup>c9</sup>The model of Hu et al. (2017)<sup>c10</sup> also considers that the continent has  
307 a constant thickness of 100 km and only includes a variation of lithospheric  
308 depth for the Amazon craton, with a thickness of 250 km. We compare SWS  
309 directions with the mantle velocity and LPO directions at different depths;  
310 150 km, 200 km, 250 km and 300 km (Fig. S22). Both models do not show  
311 large variation of the directions with depths at the continental stable region,  
312 with all directions close to E-W, on average. For having a better correla-  
313 tion with our measurements across the entire study area (Fig. S23), the

<sup>c1</sup> *Text added.*

<sup>c2</sup> We add that the models of Hu et al. (2017), are using the overriding South American plate as reference frame, as suggestion by reviewer 2.

<sup>c3</sup> *Text added.*

<sup>c4</sup> *Text added.*

<sup>c5</sup> *Text added.*

<sup>c6</sup> *Text added.*

<sup>c7</sup> *Text added.*

<sup>c8</sup> We add more detailed information about how Hu et al., (2017) calculate the LPO directions shown in Figure 7, as suggested by reviewer 2.

<sup>c9</sup> *Text added.*

<sup>c10</sup> *Text added.*

314 directions at 250 km depth were chosen for comparison. Figure 7 shows the  
 315 present velocity directions and the computed LPO orientations, both at 250  
 316 km depth, compared with the observed SWS results.<sup>c11</sup>

<sup>c11</sup> We added a paragraph explaining how the 250 km depth was chosen for comparison, and figures showing the model at different depths, as suggested by reviewer 2.

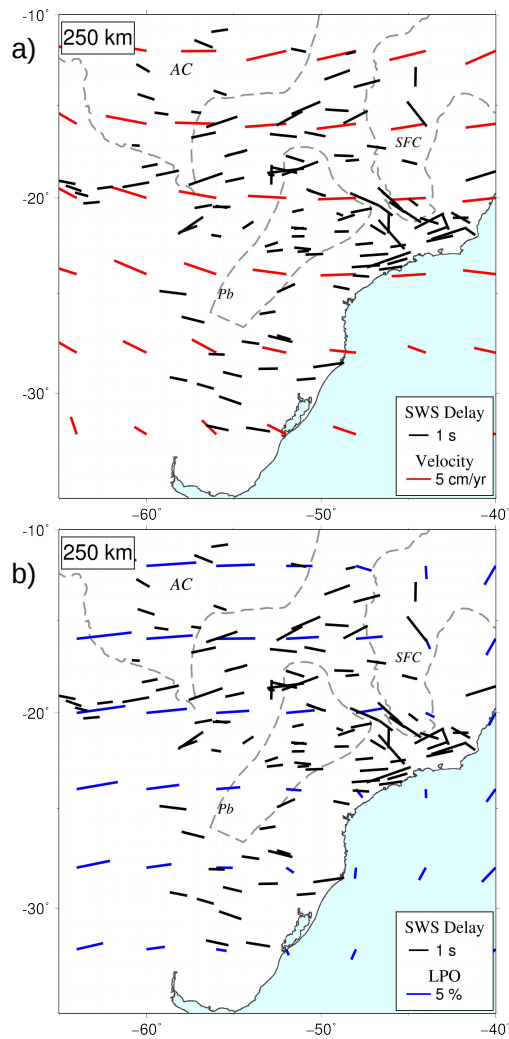


Figure 7: a) Upper mantle flow directions and LPO directions computed from TI axis, both at 250 km compared with the observed fast-polarization orientations.

317 We compare the APM, mantle velocity and LPO directions with the SWS  
 318 results in the histograms of Figure 8. The median misfit values are 15.7°,  
 319 11.8° and 11.9° respectively. This clearly shows that the slab-induced mantle  
 320 flow model is a significant improvement in explaining SWS, compared with

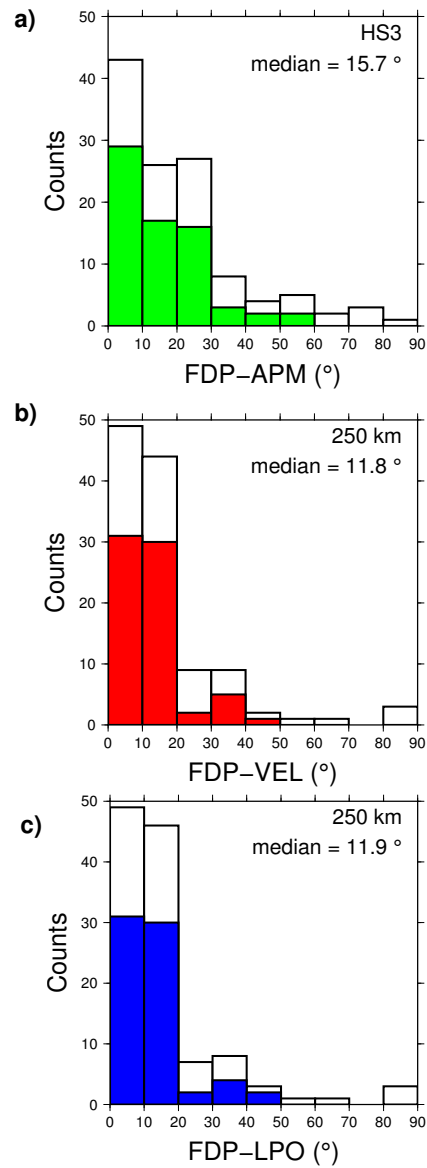


Figure 8: Histograms of the comparison of all station fast polarization orientation ( $\phi$ ) with the: a) absolute plate motion (APM) given by the HS3-NUVEL-1A model (Gripp and Gordon, 2002); b) mantle flow orientations from the model of Hu et al. (2017) at 250 km depth; c) LPO orientations from the model of (Hu et al., 2017) also at 250 km depth. Colored columns are more reliable values with measurements from 5 or more events, and white columns are all measurements.

321 the simplistic APM. Our measurements also agree with mantle flow around  
322 the Amazon craton, as predicted by the model of Hu et al. (2017), as seen  
323 in Figure 5. Further south, however, especially in the Pantanal Basin, the  
324 observed SWS fast orientations tend to be ENE-WSW, deviating from the  
325 general ESE-WNW predicted orientations in Figure 7. We propose that the  
326 observed ENE-WSW orientation may be due to flow surrounding the Parana-  
327 panema block. <sup>c1</sup> In order to visualize the deviation of the fast orientations  
328 from the Paranapanema block, we calculate the difference between the LPO  
329 model directions and our results. Values within a  $\pm 10^\circ$  difference are taken  
330 as in good agreement with the proposed model and are plotted in gray in  
331 Figure 9. The measurements with a difference higher than  $10^\circ$  clockwise,  
332 are plotted in red and the measurements with a difference more than  $10^\circ$   
333 anticlockwise are plotted in blue. South of the Paraná deep lithospheric  
334 block the fast orientation tend to deviate away (clockwise) from it. To the  
335 northwest, especially in the Pantanal basin, the fast orientations deviate an-  
336 ticlockwise, with respect with the model of Hu et al. (2017). We propose that  
337 these deviations show mantle flow deflected by the deep structures below the  
338 Paranapanema block, as we can see in Figure 9. All the three main structures  
339 (Amazon and São Francisco cratons and the Paranapanema block) seem to  
340 be diverting the flow in between them. Assumpção et al. (2006) proposed  
341 that the anisotropy orientations indicate flow around the keel of the São  
342 Francisco craton. Here, we add that the Paranapanema block also deviates  
343 mantle flow.

344 The geometry of the Paranapanema block is not known in detail. Differ-  
345 ent geological and geophysical models have been proposed (Cordani, 1984;  
346 Mantovani et al., 2005; Milani and Ramos, 2017). Different studies of surface  
347 wave tomography tend to show large velocities beneath the northern part of  
348 the Paraná basin, but with different geometries. The regional tomography  
349 of Feng et al. (2007) shows two high velocities in the northern part of the  
350 Paraná basin and a separate high velocity keel in the southern part of the  
351 São Francisco craton Figure 9-b. The proposal of Assumpção et al. (2006)  
352 of mantle flow around SFC was based on this keel. The global tomography  
353 model SL2013sv (Schaeffer and Lebedev, 2013) Figure 9-a, on the other hand,  
354 does not have resolution to separate these two keels.

355 We also observe different areas of large and small delays. Large delay  
356 times are observed in the Pantanal basin and may indicate a strong astheno-  
357 spheric channel, a more coherent flow, or a thicker asthenosphere. Further  
358 to the northeast, large delays seem to predominate between the São Fran-

<sup>c1</sup> The images are now plotted with the same reference values, and the assumptions made are still valid. Only the high velocity anomaly of the northern Parana basin -figure 10b- is not as evident as before, but it is seen in a light green shade, as suggested by reviewer 1.

359 cisco ad Amazon cratons. Small delays are generally observed beneath areas  
360 with thick lithosphere, such as the Amazon craton, and the Paranapanema  
361 block. This may indicate thinner anisotropic asthenosphere, consistent with  
362 the model of Hu et al. (2017) <sup>c1</sup>, or a different and more complex type of  
363 anisotropy, such as orientations varying with depth, or tilted fast axes of the  
364 olivine crystals (Baptiste and Tommasi, 2014).<sup>c2</sup>

365 The SFC geometry used in the mantle flow calculation of Hu et al. (2017),  
366 did not significantly change the estimated SWS orientations. For this reason,  
367 the model version used in Figure 8, Figure 7 and Figure 9 does not include  
368 the SFC. We propose that the addition of a deep keel in southern part of  
369 the SFC and the Paranapanema block should improve the fit to the observed  
370 orientations.

<sup>c1</sup> *Text added.*

<sup>c2</sup> We add a new interpretation of small delay times, as suggested by reviewer 1.

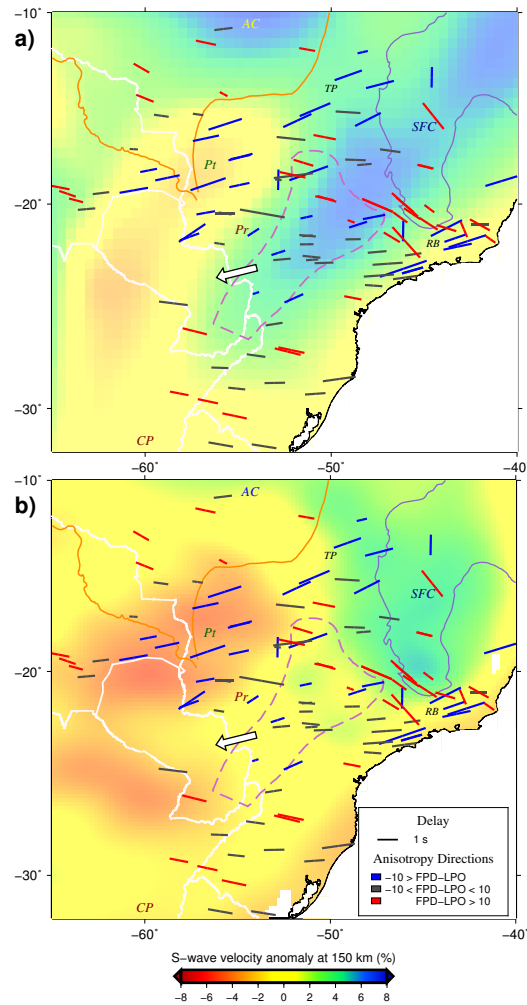


Figure 9: Same as Figure 5, with bar colors showing the difference from the LPO model of Hu et al. (2017). SWS observations which deviate more than  $10^\circ$  clockwise from the LPO directions are plotted as red bars. Deviations more than  $10^\circ$  anticlockwise are shown as blue bars. Colors indicate S-wave velocity anomalies at 150 km depth from two different tomography models: a) SL2013Sv global model of Schaeffer and Lebedev (2013), b) the regional model of Feng et al. (2007).

## 371 5. Conclusions

372 In this work we present new measurements of shear wave splitting in  
 373 the Paraná and Pantanal basins, SE Brazil, in <sup>c1</sup>an area not well sampled <sup>c1</sup> Text added.  
 374 before. In general, considering the previous and new results in the continental  
 375 midplate South America, the fast polarization orientations have an average E-

376 W trend, previously related with the absolute plate motion directions (HS3-  
377 NUVEL1A). Our results show that the subduction-induced, time dependent  
378 flow model of Hu et al. (2017) provides a much better explanation for the  
379 SWS observations, which is seen using two proxies: convection velocity and  
380 LPO at 250 km depth. The observed orientations are also consistent with  
381 the flow around the Amazon craton, predicted by their model. <sup>c2</sup> <sup>c3</sup>Our mea-  
382 surements are consistent with the proposition of cratonic block under the  
383 Parana basin, the Paranapanema block, proposed previously, diverting flow  
384 around it.

<sup>c2</sup> We also support the existence of a cratonic block under the Parana basin, the Paranapanema block, which diverts mantle flow. The small delay times observed in the Paranapanema block seem to be typical of other cratonic areas.

<sup>c3</sup> Text added.

## 385 6. Acknowledgements

386 We are thankful to the support and attention from M. Reiss with the Spli-  
387 tRacer package, L. Liu and J. Hu for providing the mantle flow model. Work  
388 supported by the FAPESP "3-Basin" grant 2013/24215-6, CAPES M.Sc.  
389 scholarship and CNPq research grant 30.6547/2013-9. We thank the "3-  
390 Basins Project Team" which made possible the production of our dataset:  
391 Felipe Neves, Luís Galhardo, José Roberto Barbosa, Cleusa Barbosa (USP,  
392 field work); Bruno Collaço, Jackson Calhau (USP, field work and data man-  
393 agement); Marcelo Bianchi, Emilia Brasílio (USP, data management and  
394 data quality); Paulo Azevedo, Marcelo Rocha (UnB, Brazil); Tiago Silva,  
395 Edna Facincani (UFMS, Brazil); Gonzalo Fernandez, Felipe Condori (OSC,  
396 Bolivia); Gerardo Sánchez, Luis Andujar (INPRES, Argentina); Rafael Fu-  
397 garazzo, Moisés Gadea, Vincent Figueres (UNA, Paraguay); Leda Sánchez,  
398 Enrique Latorres, Hernán Castro, Martín Rodríguez, Anahí Curbelo (UDE-  
399 LAR, Uruguay). Figures were prepared using the GMT software package  
400 (Wessel and Smith, 1998).

## 401 7. References

- 402 Assine, M. L. and P. C. Soares  
403 2004. Quaternary of the Pantanal, west-central Brazil. *Quaternary Inter-*  
404 *national*, 114(1):23–34.
- 405 Assumpção, M., M. Guarido, S. van der Lee, and J. C. Dourado  
406 2011. Upper-mantle seismic anisotropy from SKS splitting in the South  
407 American stable platform: A test of asthenospheric flow models beneath  
408 the lithosphere. *Lithosphere*, 3(2):173–180.

- 409 Assumpção, M., M. Heintz, A. Vauchez, and M. E. Silva  
410 2006. Upper mantle anisotropy in SE and Central Brazil from SKS split-  
411 ting: evidence of asthenospheric flow around a cratonic keel. *Earth and*  
412 *Planetary Science Letters*, 250(1):224–240.
- 413 Baptiste, V. and A. Tommasi  
414 2014. Petrophysical constraints on the seismic properties of the kaapvaal  
415 craton mantle root. *Solid Earth*, 5(1):45.
- 416 Bastow, I. D., J. Julia, A. do Nascimento, R. Fuck, T. Buckthorp, and J. Mc-  
417 Clellan  
418 2015. Upper mantle anisotropy of the Borborema Province, NE Brazil:  
419 Implications for intra-plate deformation and sub-cratonic asthenospheric  
420 flow. *Tectonophysics*, 657:81–93.
- 421 Becker, T., S. Lebedev, and M. Long  
422 2012. On the relationship between azimuthal anisotropy from shear wave  
423 splitting and surface wave tomography. *Journal of Geophysical Research:*  
424 *Solid Earth*, 117(B1).
- 425 Becker, T. W., C. P. Conrad, A. J. Schaeffer, and S. Lebedev  
426 2014. Origin of azimuthal seismic anisotropy in oceanic plates and mantle.  
427 *Earth and Planetary Science Letters*, 401:236–250.
- 428 Bianchi, M.  
429 2015. RSBR automatic sensor orientation analysis by P-wave incidence  
430 direction.
- 431 Conrad, C. P., M. D. Behn, and P. G. Silver  
432 2007. Global mantle flow and the development of seismic anisotropy: dif-  
433 ferences between the oceanic and continental upper mantle. *Journal of*  
434 *Geophysical Research: Solid Earth*, 112(B7).
- 435 Cordani, U. G.  
436 1984. *Estudio preliminar de integraçao do Pré-Cambriano com os eventos*  
437 *tectônicos das bacias sedimentares Brasileiras*, volume 15. Petrobrás, Cen-  
438 tro de Pesquisas e Desenvolvimento Leopoldo A. Miguez de Mello, Setor  
439 de Informação Técnica e Propriedade Industrial.
- 440 Debayle, E., F. Dubuffet, and S. Durand  
441 2016. An automatically updated s-wave model of the upper mantle and

- 442 the depth extent of azimuthal anisotropy. *Geophysical Research Letters*,  
443 43(2):674–682.
- 444 Dias, F., M. Assumpção, E. Facincani, G. França, M. Assine, P. AC Filho,  
445 and R. Gamarra  
446 2016. The 2009 earthquake, magnitude 4.8 mb, in the Pantanal wetlands,  
447 west-central Brazil. *Anais da Academia Brasileira de Ciências*.
- 448 Dragone, G. N., N. Ussami, M. E. Gimenez, F. G. L. Klinger, and C. A. M.  
449 Chaves  
450 2017. Western Paraná suture/shear zone and the limits of Rio Apa, Rio  
451 Tebicuary and Rio de la Plata cratons from gravity data. *Precambrian  
452 Research*, 291:162–177.
- 453 Faccenda, M. and F. Capitanio  
454 2013. Seismic anisotropy around subduction zones: Insights from three-  
455 dimensional modeling of upper mantle deformation and SKS splitting cal-  
456 culations. *Geochemistry, Geophysics, Geosystems*, 14(1):243–262.
- 457 Feng, M., S. Van der Lee, and M. Assumpção  
458 2007. Upper mantle structure of South America from joint inversion  
459 of waveforms and fundamental mode group velocities of Rayleigh waves.  
460 *Journal of Geophysical Research: Solid Earth*, 112(B4).
- 461 Fouch, M. J., K. M. Fischer, E. Parmentier, M. E. Wyssession, and T. J.  
462 Clarke  
463 2000. Shear wave splitting, continental keels, and patterns of mantle flow.  
464 *Journal of Geophysical Research: Solid Earth*, 105(B3):6255–6275.
- 465 Gripp, A. E. and R. G. Gordon  
466 2002. Young tracks of hotspots and current plate velocities. *Geophysical  
467 Journal International*, 150(2):321–361.
- 468 Heintz, M., A. Vauchez, M. Assumpção, G. Barruol, and M. Egydio-Silva  
469 2003. Shear wave splitting in SE Brazil: an effect of active or fossil upper  
470 mantle flow, or both? *Earth and Planetary Science Letters*, 211(1):79–95.
- 471 Heit, B., F. Sodoudi, X. Yuan, M. Bianchi, and R. Kind  
472 2007. An S receiver function analysis of the lithospheric structure in South  
473 America. *Geophysical Research Letters*, 34(14).

- 474 Hu, J., M. Faccenda, and L. Liu  
475 2017. Subduction-controlled mantle flow and seismic anisotropy in South  
476 America. *Earth and Planetary Science Letters*, 470:13–24.
- 477 Ismail, W. B. and D. Mainprice  
478 1998. An olivine fabric database: an overview of upper mantle fabrics and  
479 seismic anisotropy. *Tectonophysics*, 296(1):145–157.
- 480 James, D. E. and M. Assumpção  
481 1996. Tectonic implications of S-wave anisotropy beneath SE Brazil. *Geo-*  
482 *physical Journal International*, 126(1):1–10.
- 483 Julià, J., M. Assumpção, and M. Rocha  
484 2008. Deep crustal structure of the Paraná Basin from receiver functions  
485 and Rayleigh-wave dispersion: Evidence for a fragmented cratonic root.  
486 *Journal of Geophysical Research: Solid Earth*, 113(B8).
- 487 Kaminski, E., N. M. Ribe, and J. T. Browaeys  
488 2004. D-rex, a program for calculation of seismic anisotropy due to crystal  
489 lattice preferred orientation in the convective upper mantle. *Geophysical*  
490 *Journal International*, 158(2):744–752.
- 491 Mantovani, M., M. Quintas, W. Shukowsky, and B. Brito Neves  
492 2005. Delimitation of the Paranapanema Proterozoic block: a geophys-  
493 ical contribution. *Episodes-News magazine of the International Union of*  
494 *Geological Sciences*, 28(1):18–22.
- 495 Milani, E. J. and M. De Wit  
496 2008. Correlations between the classic Paraná and Cape–Karoo sequences  
497 of South America and Southern Africa and their basin infills flanking the  
498 gondwanides: Du Toit revisited. *Geological Society, London, Special Pub-*  
499 *lications*, 294(1):319–342.
- 500 Milani, E. J. and V. A. Ramos  
501 2017. Orogenias paleozóicas no domínio sul-ocidental do Gondwana e os ci-  
502 clos de subsidência da Bacia do Paraná. *Revista Brasileira de Geociências*,  
503 28(4):473–484.
- 504 Miller, M. S. and T. W. Becker  
505 2012. Mantle flow deflected by interactions between subducted slabs and  
506 cratonic keels. *Nature Geoscience*, 5(10):726–730.

- 507 Reiss, M. C. and G. Rumpker  
508 2017. Splitracer: Matlab Code and GUI for Semiautomated Analysis and  
509 Interpretation of Teleseismic Shear-Wave Splitting. *Seismological Research*  
510 *Letters*, 88(2A):392–409.
- 511 Ribe, N. M.  
512 1992. On the relation between seismic anisotropy and finite strain. *Journal*  
513 *of Geophysical Research: Solid Earth*, 97(B6):8737–8747.
- 514 Savage, M.  
515 1999. Seismic anisotropy and mantle deformation: what have we learned  
516 from shear wave splitting? *Reviews of Geophysics*, 37(1):65–106.
- 517 Schaeffer, A. and S. Lebedev  
518 2013. Global shear speed structure of the upper mantle and transition  
519 zone. *Geophysical Journal International*, 194(1):417–449.
- 520 Silver, P. G.  
521 1996. Seismic anisotropy beneath the continents: Probing the depths of  
522 geology. *Annual review of earth and planetary sciences*, 24(1):385–432.
- 523 Silver, P. G. and W. W. Chan  
524 1991. Shear wave splitting and subcontinental mantle deformation. *Journal*  
525 *of Geophysical Research: Solid Earth*, 96(B10):16429–16454.
- 526 Steinberger, B. and T. W. Becker  
527 2016. A comparison of lithospheric thickness models. *Tectonophysics*.
- 528 Ussami, N., S. Shiraiwa, and J. M. L. Dominguez  
529 1999. Basement reactivation in a sub-andean foreland flexural bulge: The  
530 Pantanal wetland, SW Brazil. *Tectonics*, 18(1):25–39.
- 531 Vinnik, L., L. Makeyeva, A. Milev, and A. Y. Usenko  
532 1992. Global patterns of azimuthal anisotropy and deformations in the  
533 continental mantle. *Geophysical Journal International*, 111(3):433–447.
- 534 Wessel, P. and W. H. Smith  
535 1998. New, improved version of generic mapping tools released. *Eos,*  
536 *Transactions American Geophysical Union*, 79(47):579–579.

# Mantle Anisotropy and Asthenospheric Flow Around Cratons in Southeastern South America

## Supplementary Material

Bruna Chagas de Melo, Marcelo Assumpção

March 2, 2018

### 1 Tables

Table S 1: New XKS splitting results calculated with the average of all individual results.  $\phi$  are fast polarization orientations and  $d\phi$  are the errors;  $\delta t$  is splitting delay time and  $d\delta t$  are the errors; N number of measurements; null values represent stations where only null measurements were available. BR and BL networks are part of the Brazilian Seismographic Network (RSBR). XC is the temporary deployment of the "3 Basins" project.

Net	Sta	Lat (°)	Lon (°)	$\phi$ (°)	$d\phi$ (°)	$\delta t$	$d\delta t$	N
BL	CLDB	-10.87	-55.80	81.8	8.4	0.86	0.21	81
BL	CNLB	-29.31	-50.85	85.4	11.8	0.98	0.24	115
BL	ITAB	-27.23	-52.13	107.0	0.0	0.72	0.00	31
BL	ITRB	-19.70	-50.36	110.6	17.3	0.90	0.29	40
BL	PLTB	-31.76	-53.60	99.1	11.1	1.24	0.29	53
BL	PTGB	-24.72	-52.01	65.8	20.9	1.01	0.29	77
BL	TRCB	-22.79	-52.64	83.5	21.2	0.83	0.32	26
BR	ARAG	-15.71	-51.81	61.6	32.4	1.50	0.48	15
BR	IPMB	-17.98	-48.21	85.0	16.6	0.69	0.24	23
BR	PDRB	-11.61	-56.73	111.8	12.7	1.01	0.30	17
BR	SALB	-15.90	-55.69	71.5	23.3	1.69	0.56	29
BR	SNDB	-11.97	-51.29	101.4	27.3	0.79	0.35	5
BR	VILB	-12.95	-60.20	120.0	37.1	0.79	0.24	13
BR	PTLB	-15.45	-59.14	98.0	3.0	0.72	0.00	9
XC	AMBA	-22.93	-54.99	null	null	null	null	10
XC	CCRS	-17.29	-57.89	null	null	null	null	3
XC	EDMB	-26.36	-54.43	null	null	null	null	2
XC	NBRS	-14.32	-55.78	108.6	15.0	0.69	0.24	4
XC	PANT	-18.99	-56.62	71.0	0.0	1.85	0.00	2
XC	RODS	-30.35	-55.20	109.0	1.0	1.20	0.16	3
XC	TBOT	-31.68	-55.94	102.0	2.8	1.18	0.22	2
XC	UNIS	-29.07	-55.07	102	8.5	0.99	0.25	6
XC	VBST	-14.53	-60.02	108.0	30.1	0.92	0.47	10

Table S 2: New XKS splitting results calculated with the joined minimization of all waveforms (under the assumption of 1 layer).  $\phi$  are fast polarization orientations and  $d\phi$  are the errors;  $\delta t$  is splitting delay time and  $d\delta t$  are the errors; N number of measurements; null values represent stations where only null measurements were available. BR and BL networks are part of the Brazilian Seismographic Network (RSBR). XC is the temporary deployment of the "3 Basins" project.

<b>Net</b>	<b>Sta</b>	<b>Lat (<math>^{\circ}</math>)</b>	<b>Lon (<math>^{\circ}</math>)</b>	$\phi(^{\circ})$	$d\phi(^{\circ})$	$\delta t$	$d\delta t$	<b>N</b>
BL	AQDB	-20.48	-55.70	99.0	5.0	0.62	0.00	26
BL	C2SB	-18.77	-52.84	97.0	8.0	0.31	0.00	11
BL	ITQB	-29.66	-56.63	106.0	4.5	0.92	0.05	30
BL	PCMB	-21.61	-51.26	86.0	5.0	0.51	0.05	22
BL	PEXB	-12.11	-48.30	77.0	4.5	0.51	0.05	17
BL	PP1b	-17.60	-54.88	77.0	2.5	0.92	0.04	22
XC	ALGR	-28.80	-53.03	89.0	4.5	1.00	0.09	9
XC	ANTJ	-22.00	-56.00	99.0	8.5	0.51	0.10	4
XC	AZCA	-28.08	-55.98	92.0	6.0	0.82	0.15	7
XC	BBLB	-18.67	-58.80	78.0	3.0	1.20	0.20	11
XC	BBRB	-18.28	-59.81	79.0	4.5	0.82	0.15	9
XC	BBSD	-17.19	-60.61	93.0	10.0	0.41	0.10	3
XC	BDQN	-20.45	-56.75	80.0	13.0	0.92	0.60	2
XC	CRSM	-27.49	-54.04	98.0	6.0	0.92	0.09	7
XC	DVLD	-16.64	-52.16	96.0	5.0	1.40	0.15	8
XC	ESFA	-24.96	-58.49	97.0	8.0	1.40	0.25	5
XC	FRBT	-25.98	-53.06	81.0	4.0	0.82	0.10	17
XC	MECA	-29.30	-58.17	101.0	3.0	0.92	0.05	4
XC	MURT	-21.66	-57.61	70.0	4.0	1.00	0.20	6
XC	POCN	-16.62	-56.73	78.0	4.5	1.30	0.25	4
XC	PTET	-15.38	-57.16	98.0	9.0	0.51	0.10	5
XC	RVDE	-19.03	-54.94	78.0	5.0	1.00	0.10	5



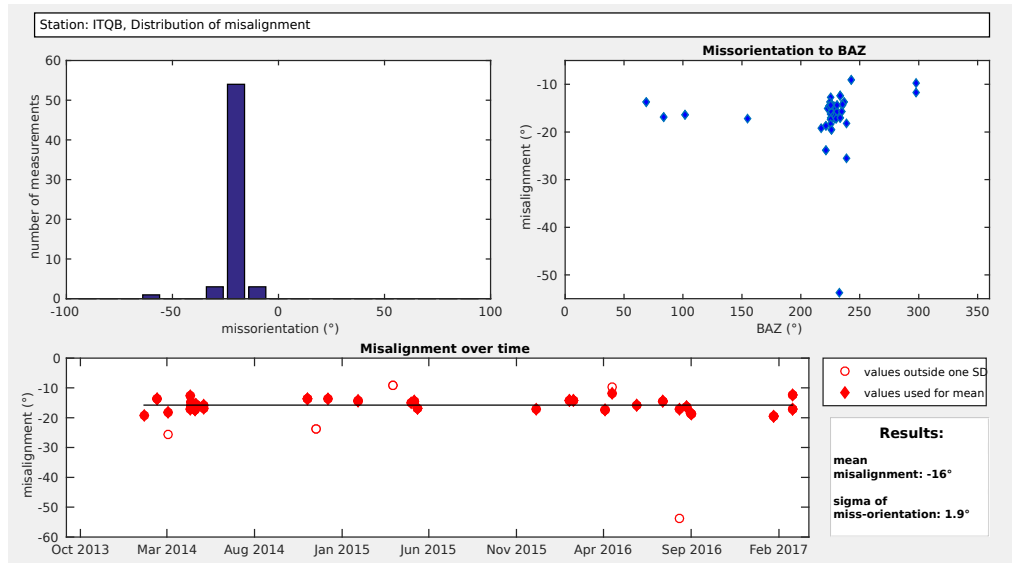


Fig. S 2: Misalignment check at station ITQB. This measure is made based on the difference between the orientation of the ellipse drawn by the XKS particle motion and the back-azimuth. This station showed a mean misalignment of  $-16^\circ$  which matched the misalignment measured with P-wave particle motions by Bianchi, 2016. For misalignments larger than  $\pm 10^\circ$  the correction was applied.

### 2.3 All measurements per station: Averaged for 1 layer

This plot helps the reader to visualize where 1 layer or other form of complex anisotropy should be considered. Despite the large variation of the anisotropy parameters with back-azimuth at some stations (see stations ITRB and PTGB, for example) we considered that the 1 layer assumption fitted well the data, and that there is not enough evidence of a 2 layer case. Where only null measurements were found, no anisotropy parameter is calculated. For all these stations, there is not sufficient data to assume if these are "null" stations with no anisotropy on the wave path.

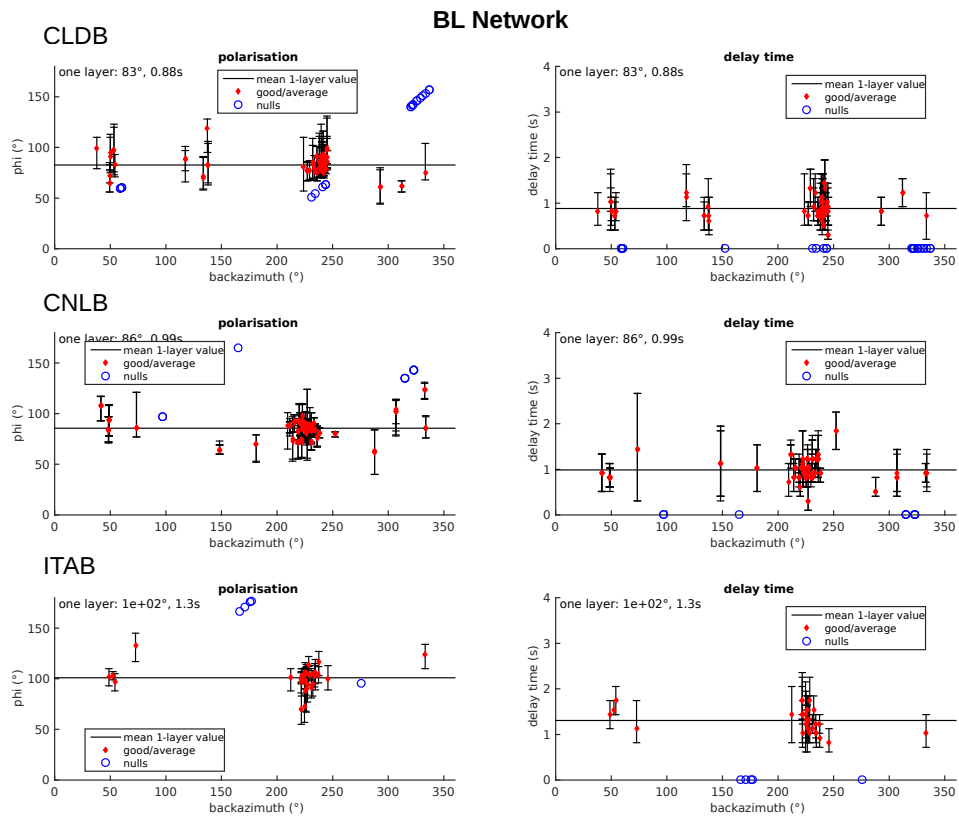


Fig. S 3: Individual measurements plotted with back-azimuth for stations CLDB, CNLB and ITAB (BL network from the RSBR). The calculated anisotropy parameters at these stations are the mean of all measurements of  $\phi$  and  $\delta t$ .

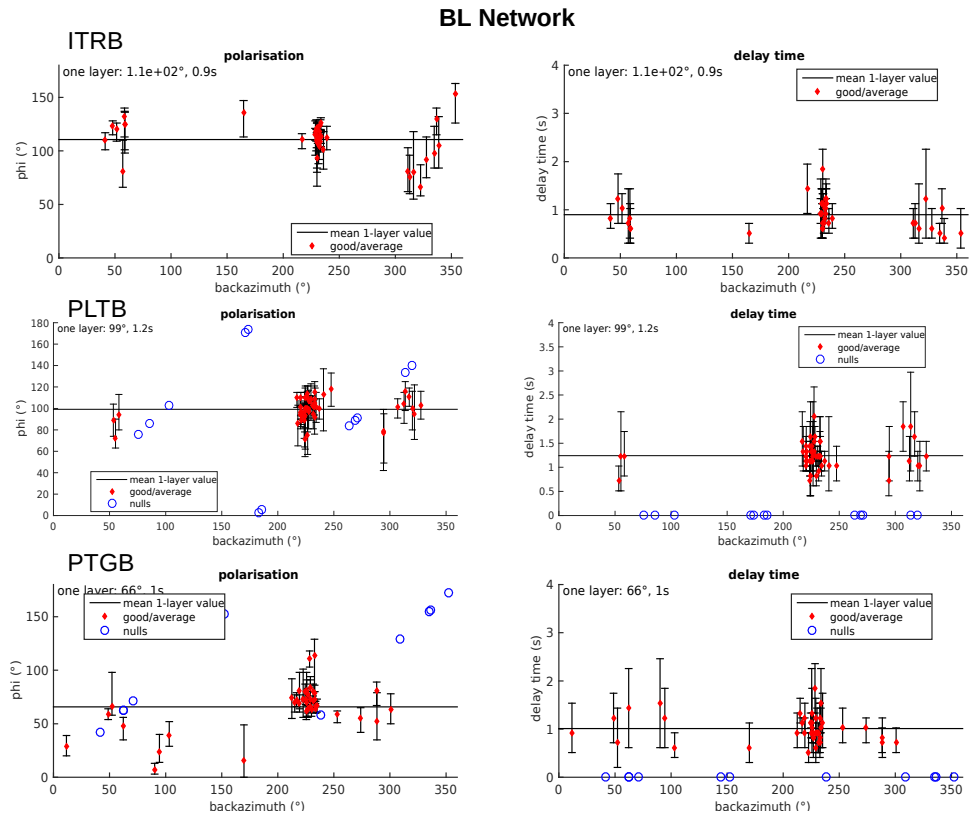


Fig. S 4: Individual measurements plotted with back-azimuth for stations ITRB, PLTB and PTGB (BL network from the RSBR). The calculated anisotropy parameters at these stations are the mean of all measurements of  $\phi$  and  $\delta t$ .

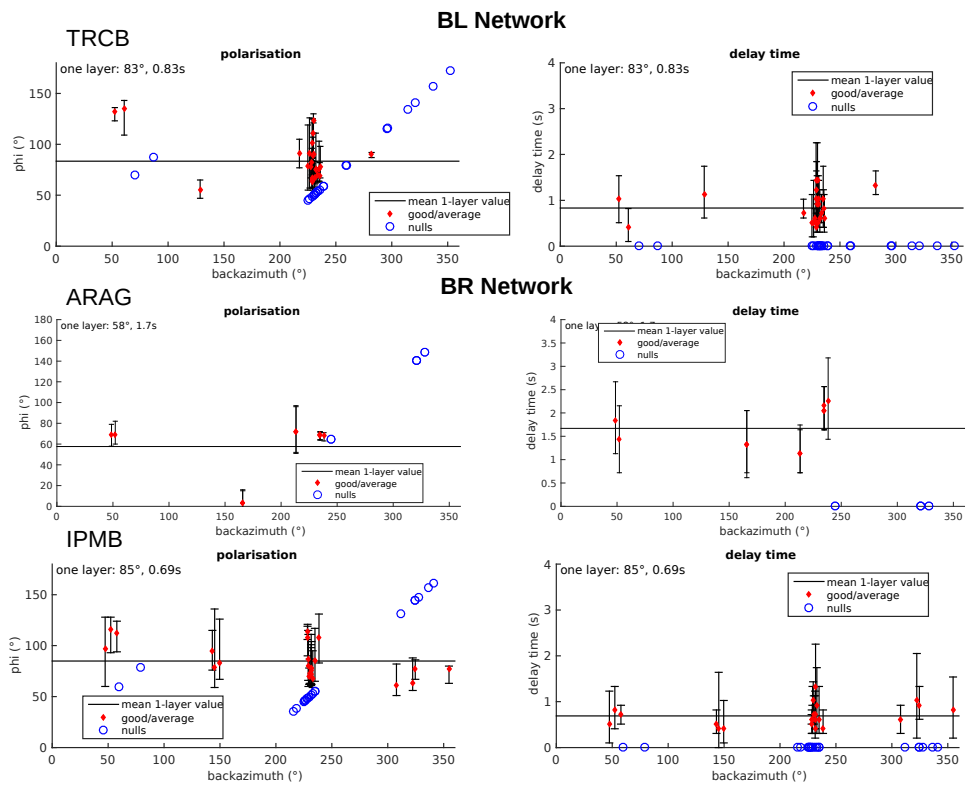


Fig. S 5: Individual measurements plotted with back-azimuth for stations TRCB, ARAG and IPMB (BL and BR networks from the RSBR). The calculated anisotropy parameters at these stations are the mean of all measurements of  $\phi$  and  $\delta t$ .

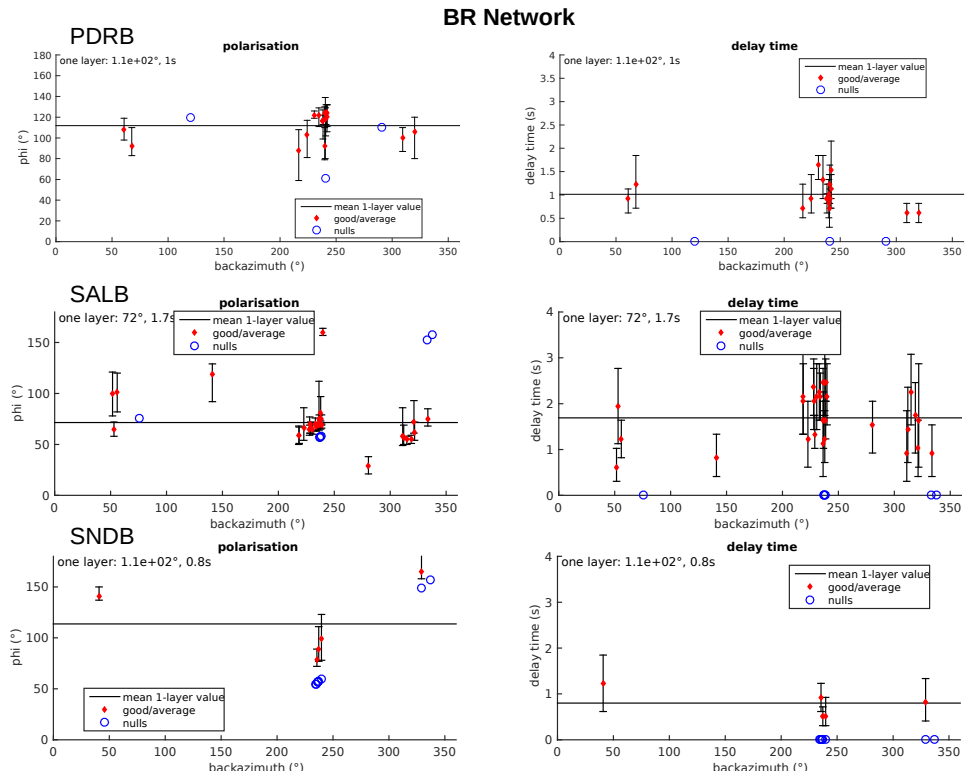


Fig. S 6: Individual measurements plotted with back-azimuth for stations PDRB, SALB and SNDB (BR network from the RSBR). The calculated anisotropy parameters at these stations are the mean of all measurements of  $\phi$  and  $\delta t$ .

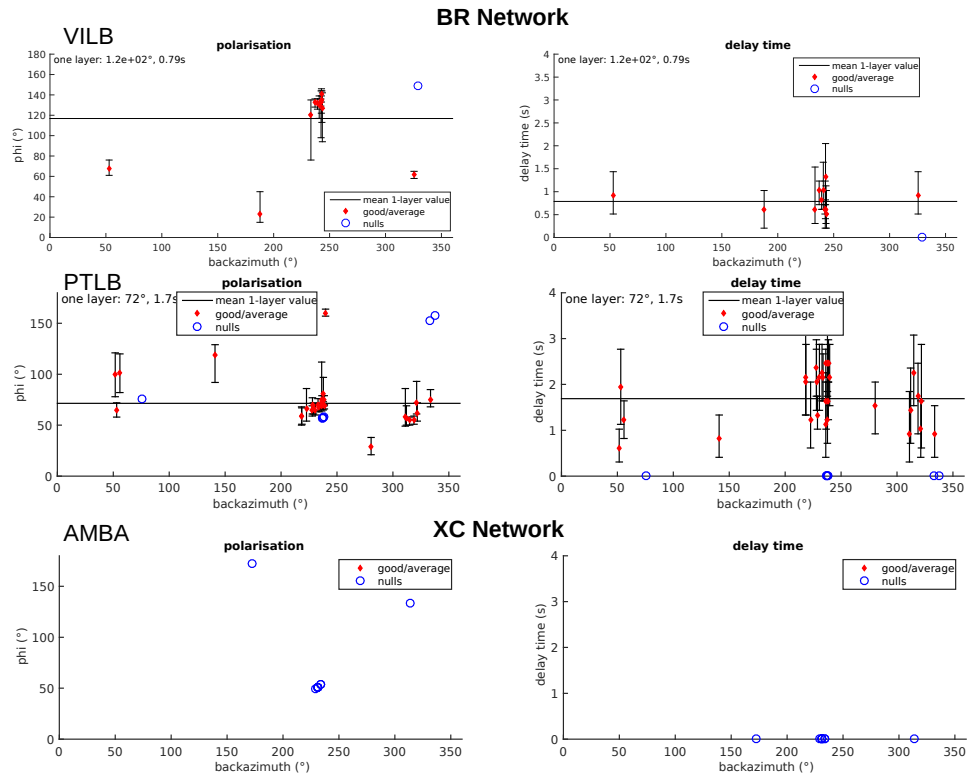


Fig. S 7: Individual measurements plotted with back-azimuth for stations VILB and PTLB (BR network from the RSBR) and station AMBA (XC network from the FAPESP "3-Basin Thematic Project"). The calculated anisotropy parameters at these stations are the mean of all measurements of  $\phi$  and  $\delta t$ .

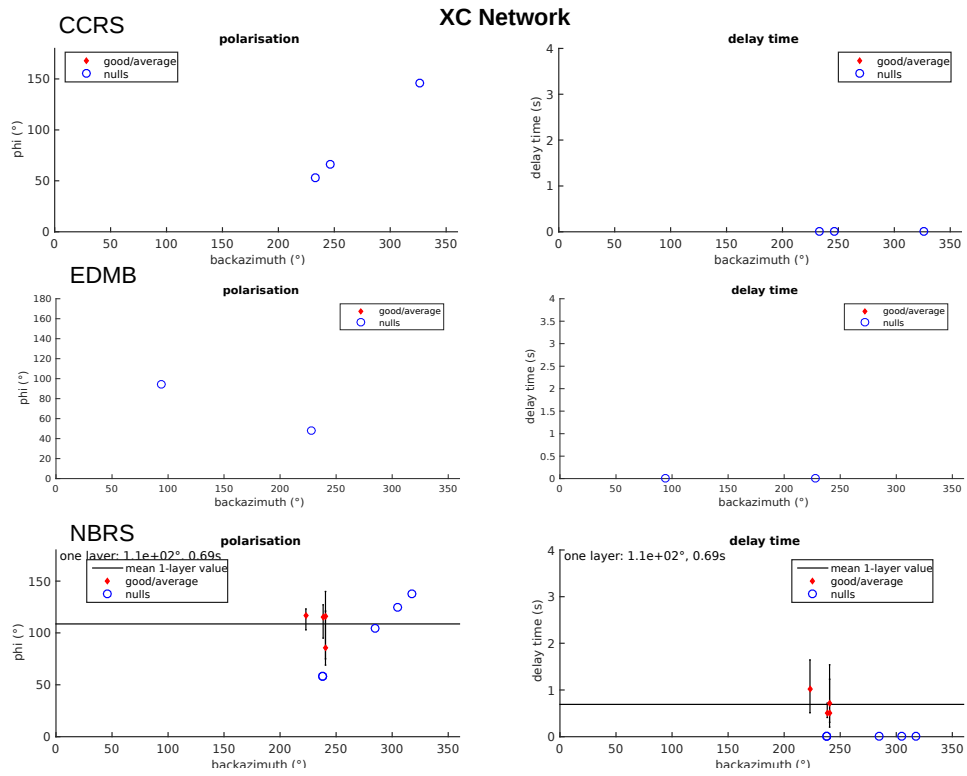


Fig. S 8: Individual measurements plotted with back-azimuth for stations CCRS, EDMB and NBRS (XC network from the FAPESP "3-Basin Thematic Project"). The calculated anisotropy parameters at these stations are the mean of all measurements of  $\phi$  and  $\delta t$ .

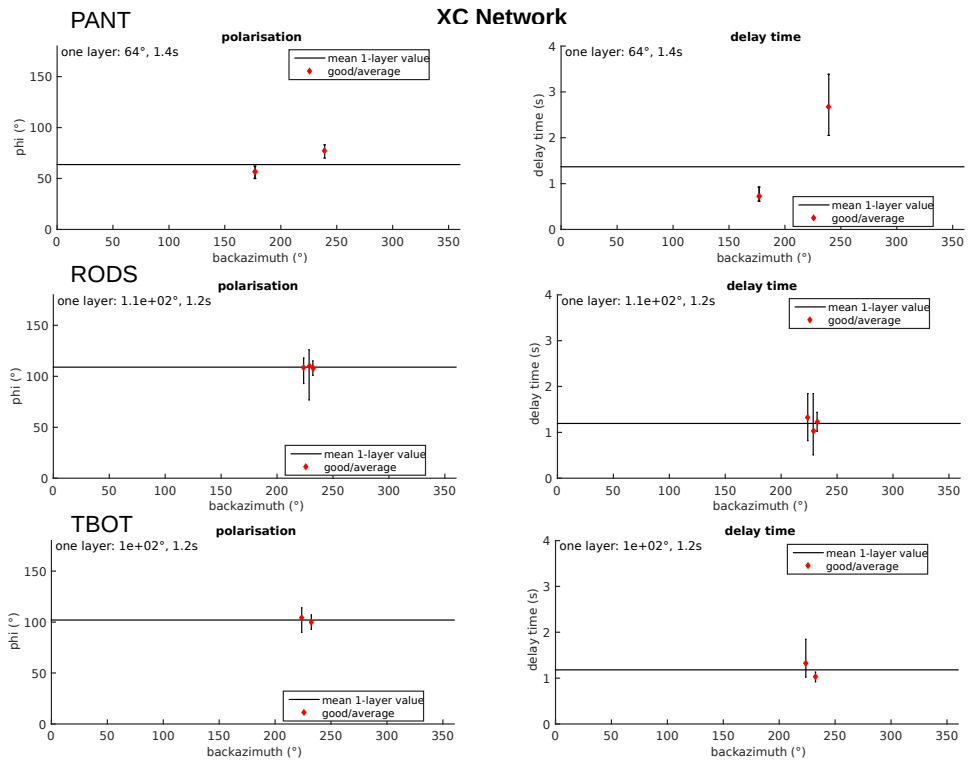


Fig. S 9: Individual measurements plotted with back-azimuth for stations PANT, RODS and TBOT (XC network from the FAPESP "3-Basin Thematic Project"). The calculated anisotropy parameters at these stations are the mean of all measurements of  $\phi$  and  $\delta t$ .

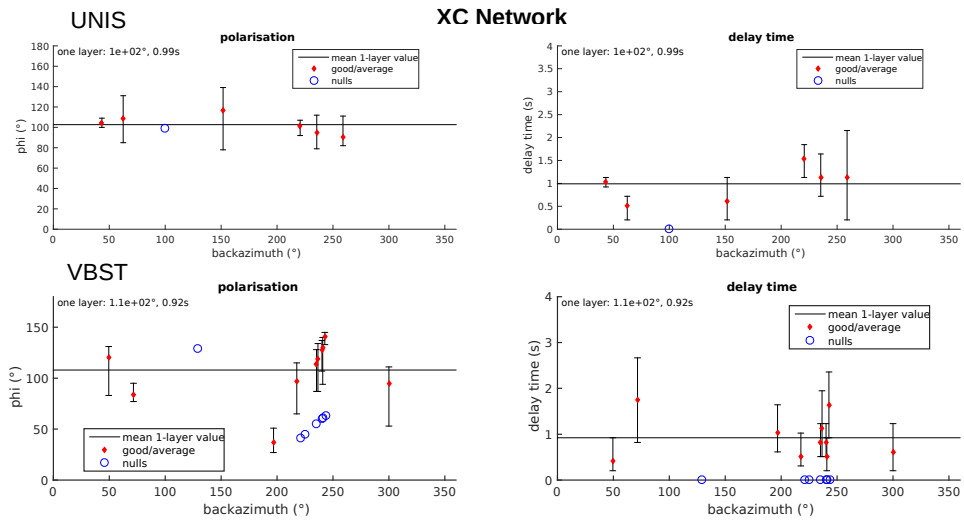


Fig. S 10: Individual measurements plotted with back-azimuth for stations UNIS and VBST (XC network from the FAPESP "3-Basin Thematic Project"). The calculated anisotropy parameters at these stations are the mean of all measurements of  $\phi$  and  $\delta t$ .

## 2.4 All measurements per station: Joint Waveform Inversion for 1 layer

At these stations, a smaller variability of the parameters with back-azimuth is observed, and a joint waveform inversion for one layer was performed.

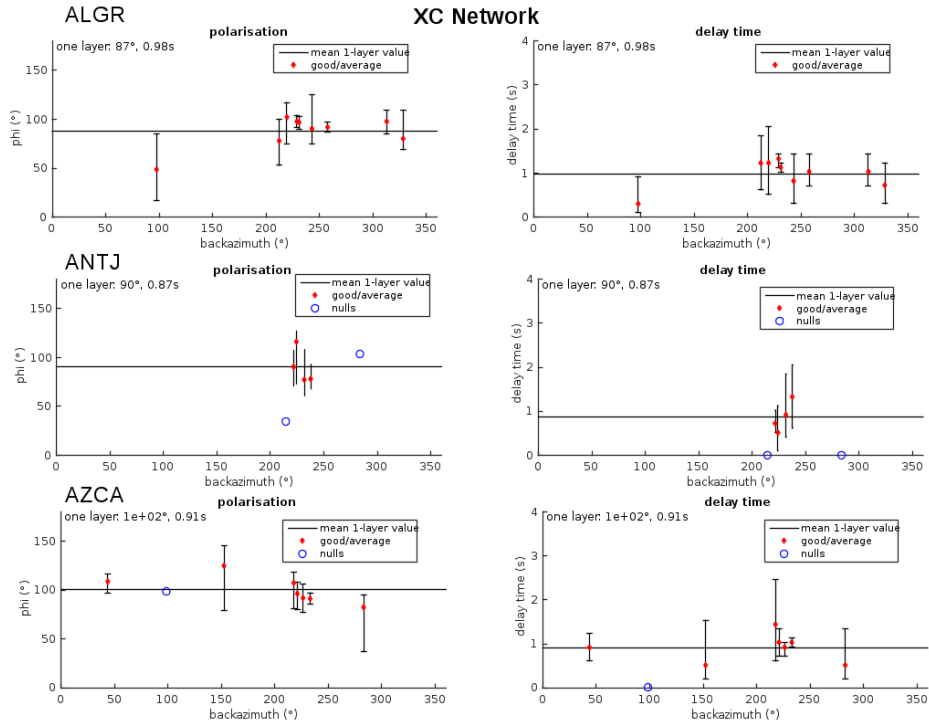


Fig. S 11: Individual measurements plotted with back-azimuth for stations ALGR, ANTJ and AZCA (XC network from the FAPESP "3-Basin Thematic Project").

## 2.5 2 layer anisotropy

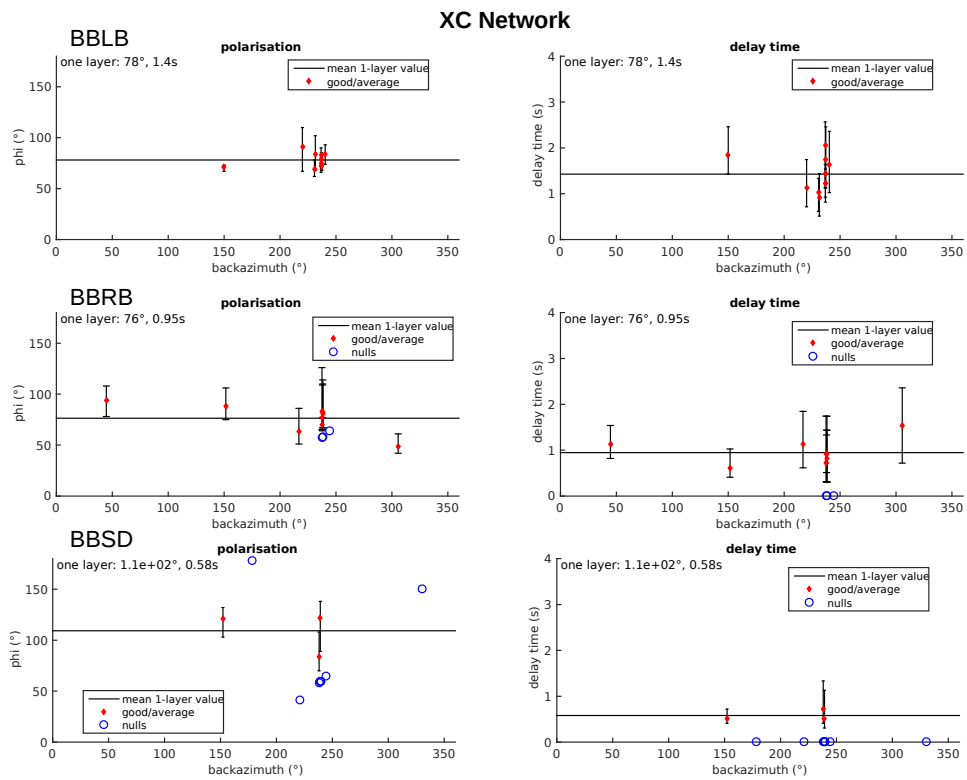


Fig. S 12: Individual measurements plotted with back-azimuth for stations BBLB, BBRB and BBSD (XC network from the FAPESP "3-Basin Thematic Project").

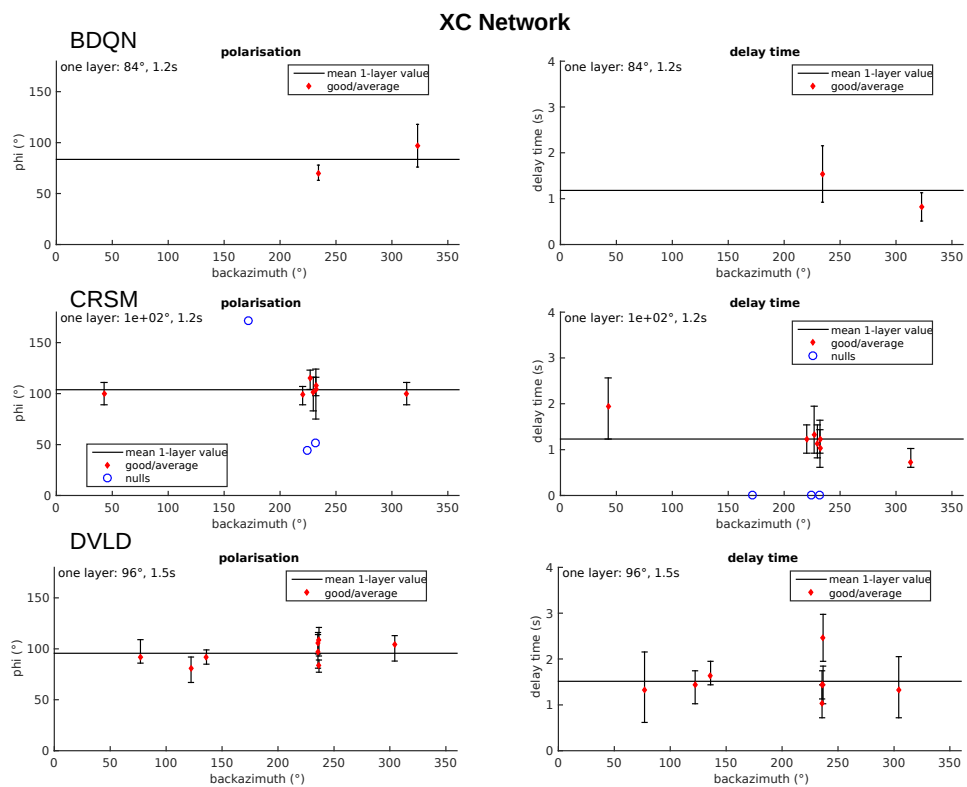


Fig. S 13: Individual measurements plotted with back-azimuth for stations BDQN, CRSM and DVLD (XC network from the FAPESP "3-Basin Thematic Project").

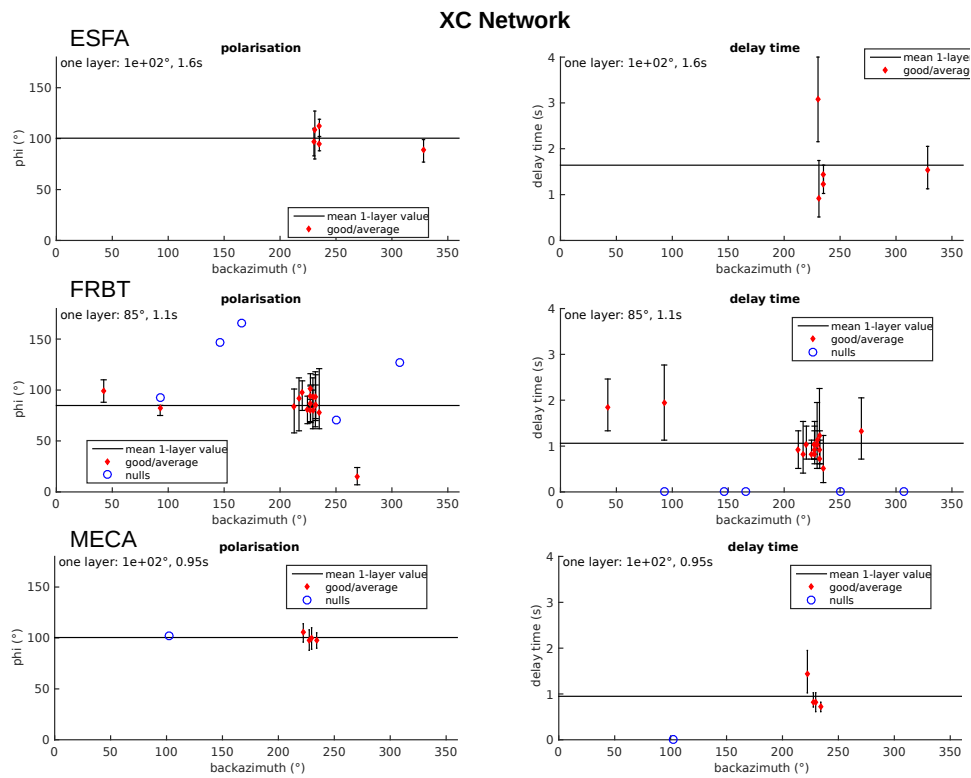


Fig. S 14: Individual measurements plotted with back-azimuth for stations ESFA, FRBT and MECA (XC network from the FAPESP "3-Basin Thematic Project").

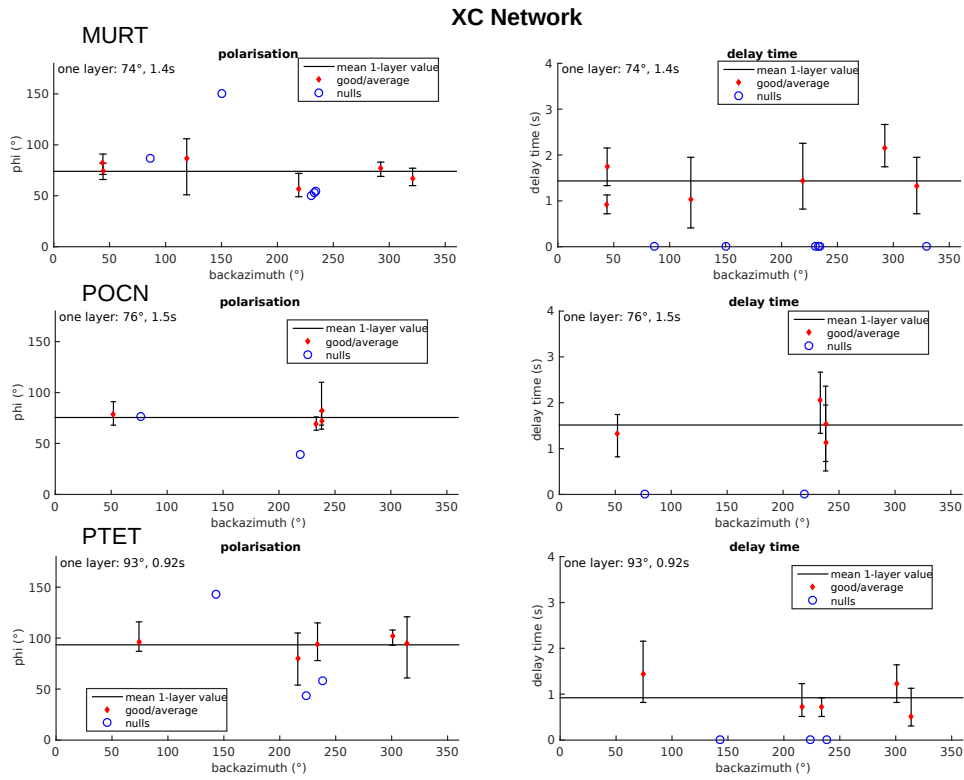


Fig. S 15: Individual measurements plotted with back-azimuth for stations MURT, POCN and PTET (XC network from the FAPESP "3-Basin Thematic Project").

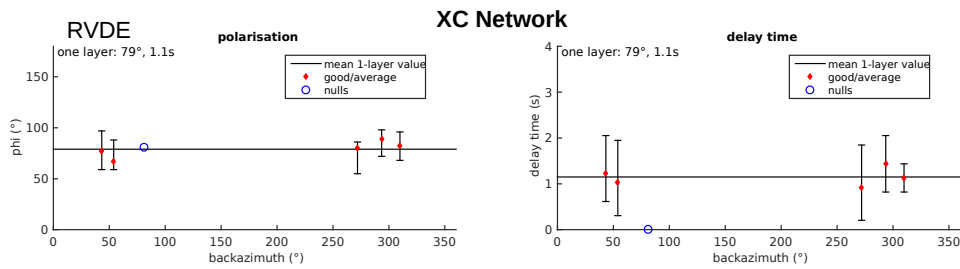


Fig. S 16: Individual measurements plotted with back-azimuth for stations RVDE (XC network from the FAPESP "3-Basin Thematic Project").

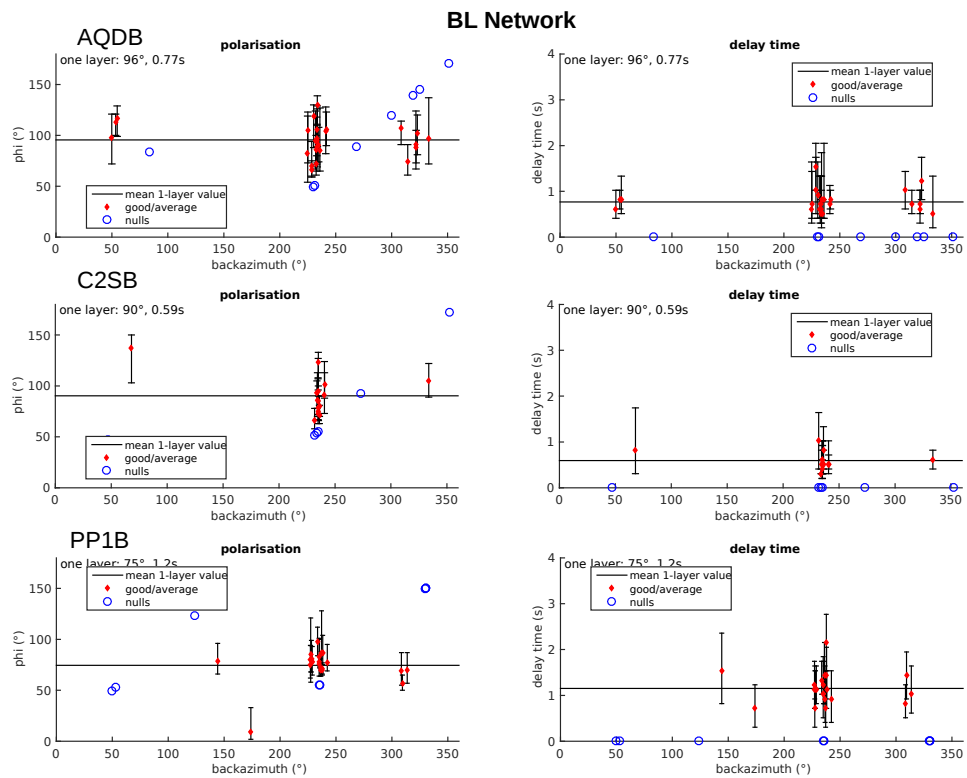


Fig. S 17: Individual measurements plotted with back-azimuth for stations AQDB, C2SB and PP1B (BL network from the RSBR).

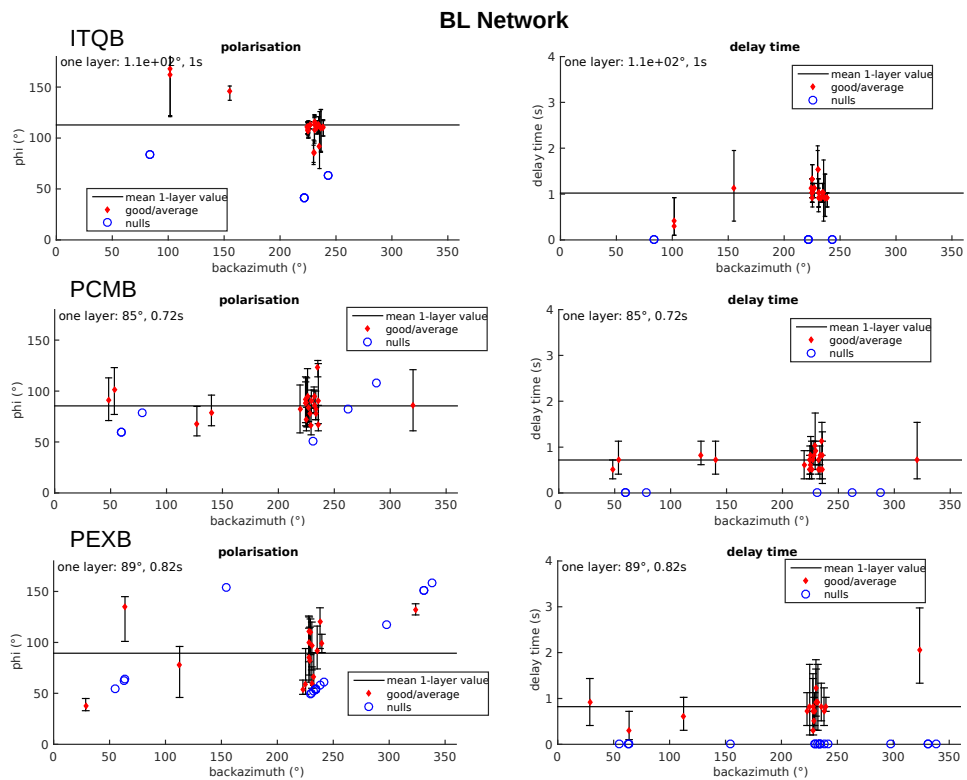


Fig. S 18: Individual measurements plotted with back-azimuth for stations ITQB, PCMB and PEXB (BL network from the RSBR).

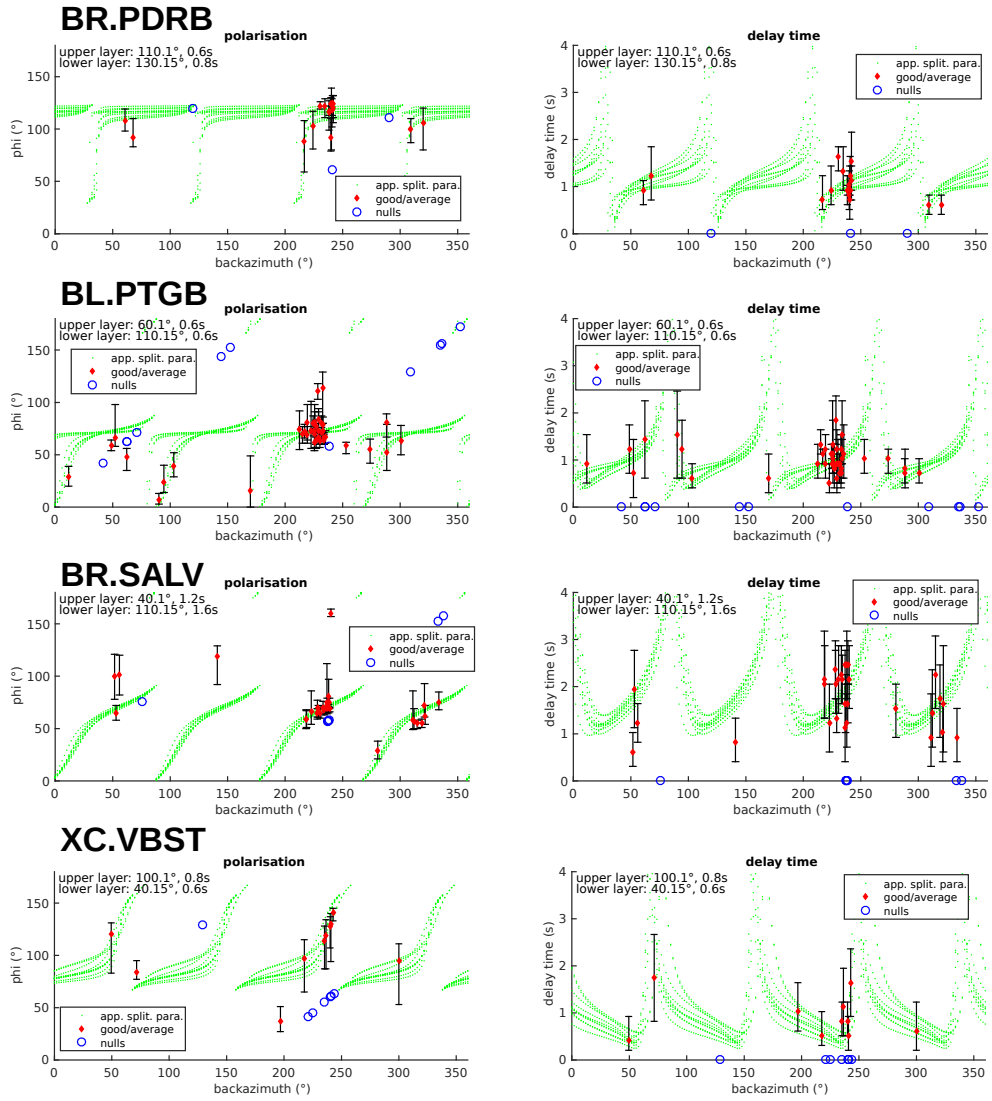


Fig. S 19: Stations where a 2 layer case was investigated.

## 2.6 Models at different depths

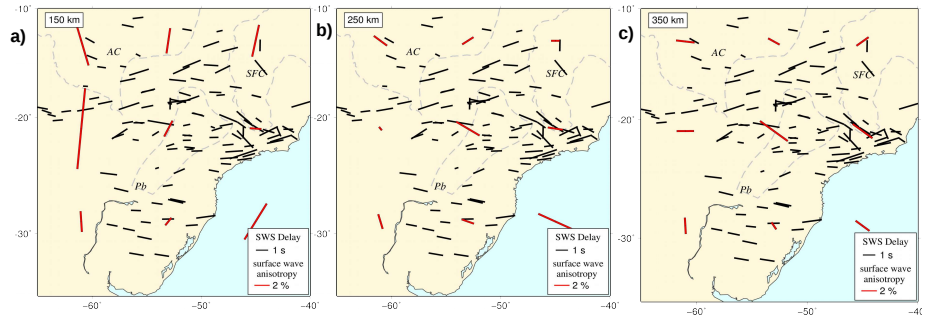


Fig. S 20: Surface wave anisotropy directions at different depths, compared to the SWS anisotropy directions. a) At 150 km depth; b) At 250 km depth; c) 350 km depth.

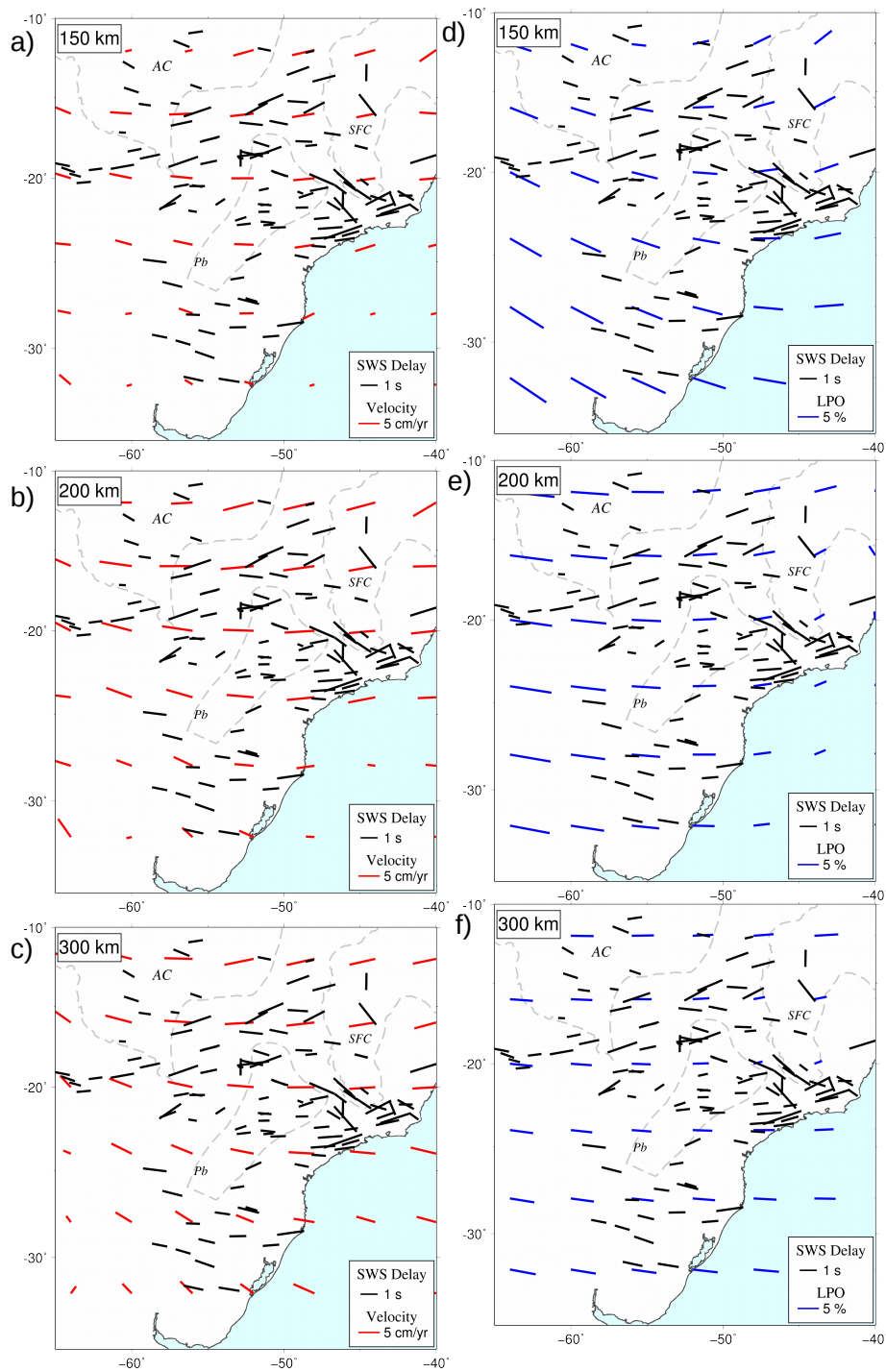


Fig. S 21: a), b) and c) are subduction induced mantle flow velocity directions at 150 km, 200 km and 300 km depth, respectively. d), e) and f) are LPO directions computed from TI axis also at at 150 km, 200 km and 300 km depth, respectively.

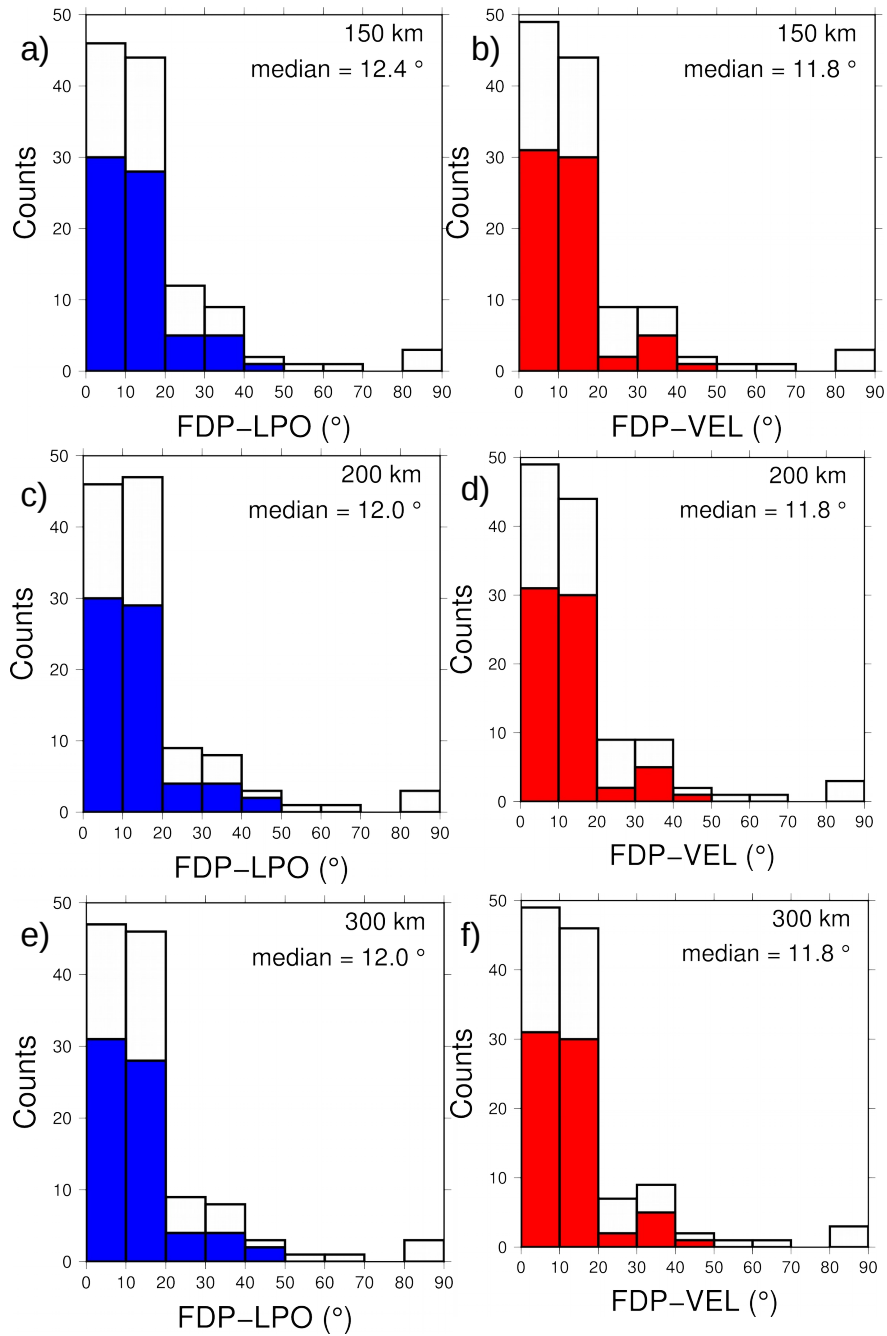


Fig. S 22: Histograms of the comparison of all station fast polarization orientations with LPO directions computed from TI axis also at 150 km, 200 km and 300 km depth, respectively. b), d) and f) are the comparison with subduction induced mantle flow velocity directions also at 150 km, 250 km and 300 km depth, respectively. Colored columns are more reliable values with measurements from 5 or more events, and white columns are all measurements.

# Chapter 3

## Additional Results and Discussion

Beyond the results presented at Chapter 2, now we add 20 new measurements at the northern part of Brazil from  $10^{\circ}$  S to  $5^{\circ}$  N in an area poorly sampled before. The new measurements also have a general ENE-WSW pattern, with some stations deviating to a ESE-WNW orientation. Furthermore, stations in northwestern Brazil (not plotted here), and northeastern Brazil mainly have null results, as already observed by Bastow et al. (2015). We first compare the SWS fast orientations with the surface wave azimuthal global anisotropy orientations at 300 km depth from Debayle, Dubuffet, and Durand (2016), Figure 3.1.

There is some similarity between the orientations at the northern and western boundaries, with all SWS orientations tending to be ENE-WSW and the surface wave anisotropy orientations with a more accentuated NE-SW orientation. These areas have less influence of the lithospheric thickness variation caused by the cratons, and the surface wave anisotropy orientations reflect mainly the large scale mantle flow direction at 300 km depth. Therefore, the SWS orientations at these regions may be due only to upper mantle flow. At the central part of northern Brazil, the SWS orientations do not correlate with the surface wave anisotropy orientations, meaning that a smaller scale change in anisotropy is present. Figure 3.2 we see the main basement faults mapped at Brazilian territory by CPRM (Brazilian Geological Services). Beyond the general ENE-WSW orientations of the SWS measurements, a second pattern of orientations trending ESE-WNW is present (blue circles in Figure 3.2) which may correlate with some of the SW-NE

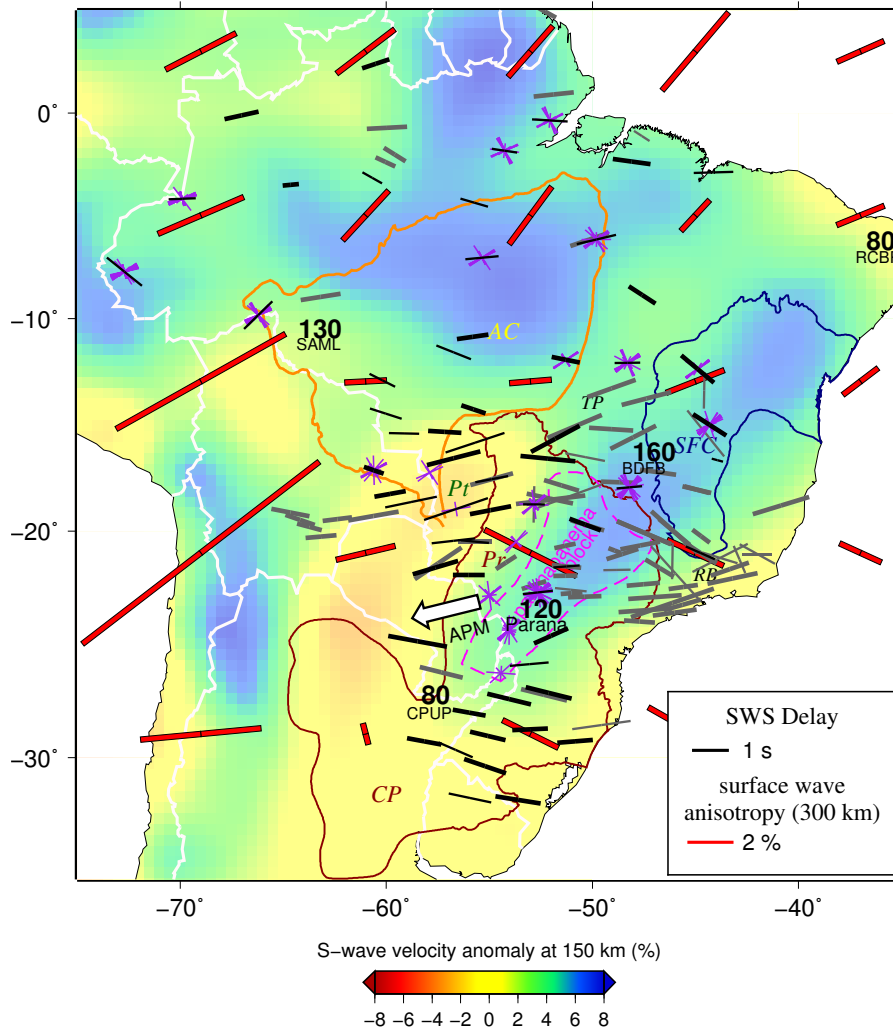


Figure 3.1: All SWS fast directions from this study (black bars) and other published results (gray bars). The bar lengths indicate delay time and good/average qualities of SWS are indicated by thick and thin bars. Red bars are surface wave azimuthal anisotropy directions at 300 km depth. Colors indicate S-wave velocity anomalies at 150 km depth from the surface-wave tomography model SL2013Sv. The white arrow indicates the absolute plate motion in the hotspot reference frame HS3-NUVEL1A. Colored contours are boundaries of major provinces. Null bars (purple bars) are plotted at stations where few or no measurements were found. Bold numbers denote lithosphere/asthenosphere depth from S-wave receiver functions.

major fault orientation of the basement.

In these areas, the SWS anisotropy directions may be due only to frozen anisotropy imprinted at the lithosphere, from past tectonic events, or they can be a compound effect of the asthenospheric anisotropy, generated by mantle flow, plus the lithospheric frozen anisotropy. Baptiste and Tommasi (2014) argues that small delays and null SWS measurements may result from vertical variations of seismic anisotropy, which could be the reason of the observed small delays and many null results in northern Brazil.

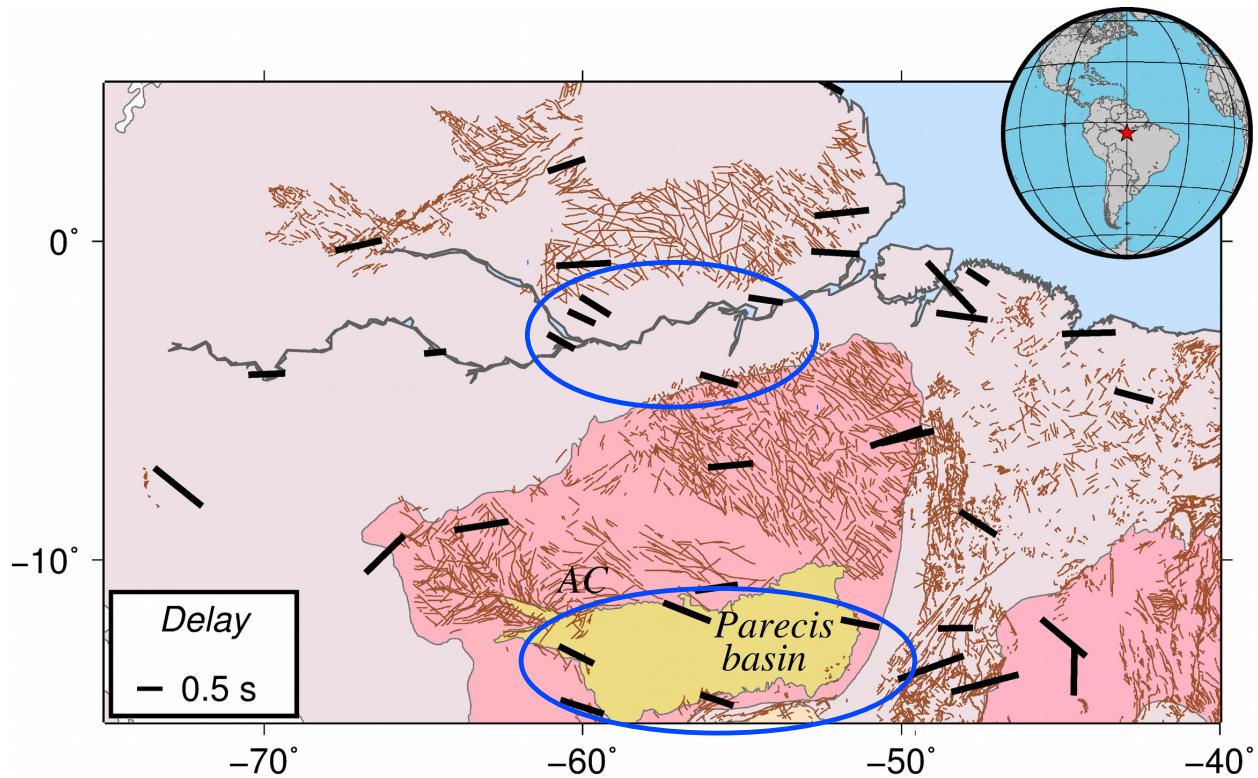


Figure 3.2: SWS orientations compared with the main faults mapped at Brazilian territory. Blue ellipses are the areas where the SWS measurements show a general ESE-WNE direction. In few stations there is a indicative of agreement of the SWS orientation with the direction of the fault alignment. AC: Amazon Craton.

### 3.1 Comparison with Different Anisotropy Proxies

In this section we compare all SWS measurements of this study with three different proxies of anisotropy: convection velocity, computed LPO directions from TI axis, and predicted SWS, all from the model of Hu, Faccenda, and Liu (2017), shown in Figure 3.3.

LPO and velocity models were already discussed at Chapter 2. To calculate the synthetic SKS splitting, Hu, Faccenda, and Liu (2017) use the software package FSTRACK from Becker et al. (2006). The code gathers the elastic tensors of all upper mantle aggregates and stack them into layers below the station. Synthetic seismograms are calculated for various azimuths and distances, and filtered to the XKS frequency band of 0.1 to 0.3 Hz. Finally, the XKS splitting parameters are determined by the cross correlation method of Menke and Levin (2003).

We calculate the orientation difference of mantle velocity, LPO orientation and synthetic SWS

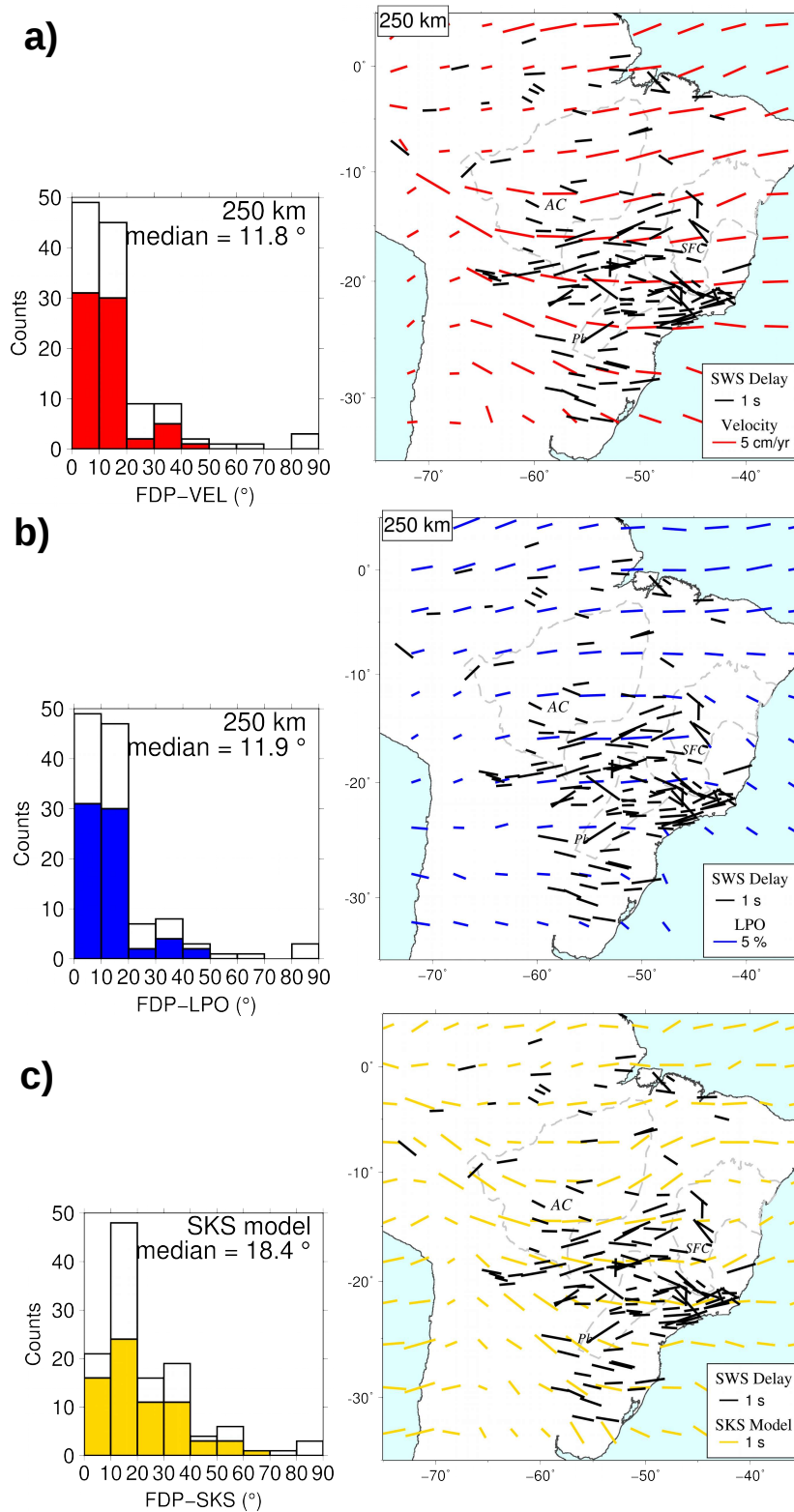


Figure 3.3: Upper mantle flow directions (a) and LPO directions computed from TI axis (b), both at 250 km compared with the observed fast-polarization orientations (black bars) and their respective histograms of the difference between the SWS direction and the model. (c) comparison of the observed SWS fast directions with the predicted SKS, with its respective histogram (Hu, Faccenda, and Liu, 2017)

with all SWS measurements of this study in the histograms of Figure 3.3. The median misfit values are  $11.8^\circ$ ,  $11.9^\circ$  and  $18.9^\circ$  respectively. The addition of the new data did not make a big change in the median values of the difference between the SWS measurements and the velocity and LPO proxies. However we note that in the Amazon region, the SWS anisotropy orientations and delays correlate slightly better with the mantle velocity directions and intensities, compared with LPO (Figure 3.3-a,b). We also show that the synthetic SWS direction do not provide a good fit to the data (Figure 3.3-c), although it should be the best estimate, theoretically. Perhaps, this worse misfit suggests higher uncertainties in the calculation of the synthetic SKS fast directions in Hu, Faccenda, and Liu (2017).

## 3.2 Two Layer Anisotropy

We now test the 2-layer anisotropy model at stations that showed larger variation of the anisotropy parameters with back-azimuth (Figure 3.4). Moreover, they had to exhibit a good back-azimuthal distribution, so that the  $\pi/2$  periodicity could be observed. Figure 3.5 shows the 1-layer and 2-layer anisotropy parameter found at each station. Black bars are the orientations of the lower layer of the 2-layer model, purple bars are the directions of the upper layer, and bars in green are the orientations of the 1-layer model. The length of the bars indicates the delay time. We want to compare whether these directions correlate with lithospheric frozen anisotropy, which can be related to the fault alignment trend observed at the surface, and with asthenospheric properties, such as mantle velocity and LPO alignment.

At station PDRB both models show a SW-NE orientation. However both the lower and upper layer have similar orientations of the nearby faults. At this station frozen anisotropy could have a larger contribution than asthenospheric flow. This could be due to a thin asthenosphere below a thick craton. At station VBST the lower layer has the same orientation as the surface wave anisotropy and upper layer in the same orientation as the mantle flow. At station SALB the lower layer has a orientation close to the mantle velocity orientation, and the upper layer has the same orientation of the local fault trend. Finally, at station PTGB the lower layer

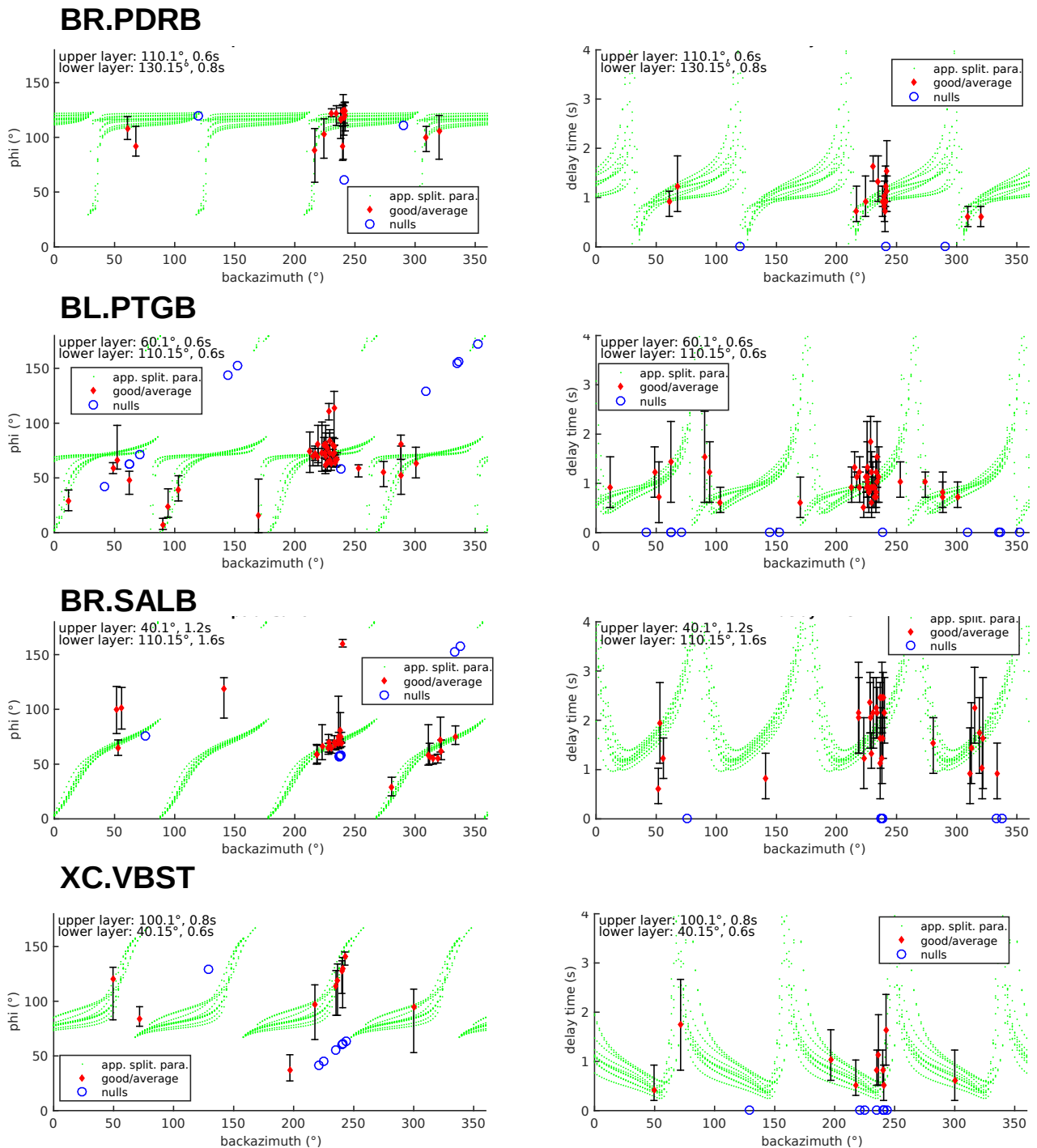


Figure 3.4: Two-layer anisotropy results at stations PDRB, PTGB, SALB and VBST plotted with back-azimuth. The curves in green are the 10 best fit models relating the 1 layer apparent parameters to the 2-layer parameters, by the method of Silver and Savage (1994).

orientation is also close to the mantle velocity orientation, but no clear fault trend can be correlated with the upper. These last two stations show some evidence of 2-layer of anisotropy

Differently from the data analyzed at Chapter 2, which showed no correlation with lithospheric

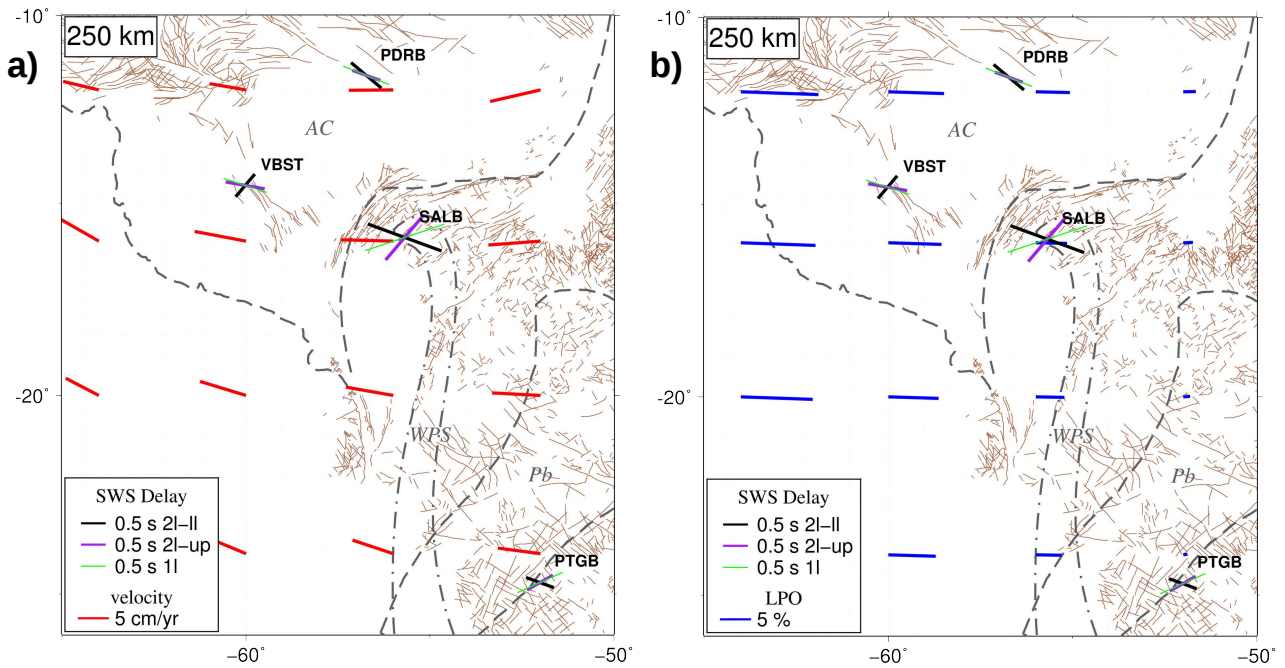


Figure 3.5: Stations where a 2-layer inversion was calculated compared with a) velocity directions and b) LPO from TI axis, both at 250 km depth, and main fault directions in brown. Black bars are anisotropy directions of the lower layer, purple bars are anisotropy directions of the upper layer and green bars are the 1-layer anisotropy directions. AC: Amazon craton; WPS: Western Parana Suture; Pb: Paranapanema block

structures (as shown by the comparison with the basement fault trends), now we have some indication of frozen lithospheric anisotropy at the central part of northern Brazil, with a general NW-SE trend. In addition, we now compare all the new data with the directions of mantle flow velocity, computed LPO and synthetic SKS from the model of Hu, Faccenda, and Liu (2017). The addition of the SWS measurements of the northern region did not significantly change the fit to the mantle flow velocities and computed LPO (median misfit of  $\approx 12^\circ$ , Figure 3.3). We also tested a 2-layer model for a few stations, and by comparing these results with different mantle models and basement fault directions we find that stations SALB and PTGB show some evidence of a 2-layer anisotropy, with the lower layer orientations having a better correlation with the mantle velocity directions. Altogether the Amazon region does not have enough stations with good measurements for a clear definition of the anisotropy pattern. More stations and data are necessary for a more conclusive interpretation.

# Bibliography

- Baptiste, V. and A. Tommasi (2014). “Petrophysical constraints on the seismic properties of the Kaapvaal craton mantle root”. In: *Solid Earth*. ISSN: 18699510. DOI: 10.5194/se-5-45-2014.
- Bastow, I. D. et al. (2015). “Upper mantle anisotropy of the Borborema Province, NE Brazil: Implications for intra-plate deformation and sub-cratonic asthenospheric flow”. In: *Tectonophysics*. ISSN: 00401951. DOI: 10.1016/j.tecto.2015.06.024.
- Becker, T. W. et al. (2006). “Mantle flow under the western United States from shear wave splitting”. In: *Earth and Planetary Science Letters*. ISSN: 0012821X. DOI: 10.1016/j.epsl.2006.05.010.
- Debayle, E., F. Dubuffet, and S. Durand (2016). “An automatically updated S-wave model of the upper mantle and the depth extent of azimuthal anisotropy”. In: *Geophysical Research Letters*. ISSN: 19448007. DOI: 10.1002/2015GL067329.
- Hu, J., M. Faccenda, and L. Liu (2017). “Subduction-controlled mantle flow and seismic anisotropy in South America”. In: *Earth and Planetary Science Letters*. ISSN: 0012821X. DOI: 10.1016/j.epsl.2017.04.027.
- Menke, W. and V. Levin (2003). “The cross-convolution method for interpreting SKS splitting observations, with application to one and two-layer anisotropic earth models”. In: *Geophysical Journal International*. ISSN: 0956540X. DOI: 10.1046/j.1365-246X.2003.01937.x.
- Silver, P. G. and M. K. Savage (1994). “The Interpretation of Shear Wave Splitting Parameters In the Presence of Two Anisotropic Layers”. In: *Geophysical Journal International*. DOI: 10.1111/j.1365-246X.1994.tb04027.x.

# Chapter 4

## Conclusion

### 4.1 Final Conclusions

In this work we present new measurements of shear wave splitting in Brazil and some neighboring countries, in areas not well sampled before. In general, considering the previous and new results in the continental midplate South America, the fast polarization orientations have an average E-W trend, previously related with the absolute plate motion directions (HS3-NUVEL1A). Our results show that the subduction-induced, time dependent flow model of Hu et. al., (2017), provides a much better explanation for the SWS observations, which is seen using three proxies: convection time dependent mantle velocity and computed LPO from TI axis at 250 km depth. We also compare the results with the computed SWS directions of Hu et. al., (2017), however those do not provide a good fit to the data. Most observed orientations are consistent with the flow around the Amazon craton, predicted by their model. We also support the existence of a cratonic block under the Paraná basin, the Paranapanema block, which diverts mantle flow. The small delay times observed in the Paranapanema block seem to be typical of other cratonic areas, such as the Amazon craton.

## 4.2 Summary of Achievements

During these two years of M.Sc. research, several activities and achievements have been developed. Beyond the paper entitled "Mantle Anisotropy and Asthenospheric Flow Around Cratons in Southeastern South America" presented here as body of this dissertation, this work has been presented at two conferences. On the 21st of April of 2017 this work was presented as the poster "Asthenospheric Flow Around the Paraná Basin Cratonic Nucleus Measured with SKS splitting" at the "XXVII Reunión Científica de la Asociación Argentina de Geofísicos y Geodestas" in La Plata, Argentina, and was awarded as the best poster presentation of the Earth's Interior Thematic Section. And on the 14th of November of 2017 "Mantle Anisotropy And Asthenospheric Flow Around Cratons In Southeastern South America" was presented at the II Simpósio Brasileiro de Sismologia at João Pessoa, Brazil. Moreover, an abstract entitled "SKS Seismic Anisotropy Observations in Mid-Plate South America: Investigating Mantle Flow and Effects of Cratonic Keels" has been accepted at this year's Seismology of the Americas meeting at Miami, US.

## 4.3 Future Work

The Brazilian Seismographic Network now counts with a large number of stations and high amount of data. This dissertation can serve as an initial study of the anisotropy in the stable South American platform, and with more data availability and focus in this area, expanding on these findings will be crucial to our understanding of the region in depth.

Although a single horizontal layer of anisotropy is a common simplified hypothesis in shear wave splitting studies, one makes significant assumptions about the orientation and symmetry of anisotropy, while also simplifying the XKS ray paths as being vertically incident. Given the variability of the shear wave splitting measurements in this area, we can say that there are regions where a more detailed study, focusing on the analyses of other anisotropic models can reveal anisotropic structures not yet observed. The stations in Brazil and the stations of the temporary FAPESP "3-Basin" deployment provide a unique opportunity to test different

---

models of anisotropy forming mechanisms in the vicinity of a cratonic margin. It is plausible to assume that there are both a lithospheric and an asthenospheric components to the upper mantle anisotropy. Therefore, a natural recommendation for future work is to expand the interpretations to these more complex anisotropy scenarios. Older stations with larger datasets should provide enough back-azimuthal coverage to effectively test the 2-layer hypothesis or even other more complex anisotropic structures.

# Appendix A

## Supplementary Material

Table A.1: Complete list of the new XKS splitting results calculated with the average of all individual results.  $\phi$  are fast polarization orientations and  $d\phi$  are the errors;  $\delta t$  is splitting delay time and  $d\delta t$  are the errors; N is the number of measurements; null values represent stations where only null measurements were available. BR and BL networks are part of the Brazilian Seismographic Network (RSBR). XC is the temporary deployment of the "3 Basins" project.

Net	Sta	Lat ( $^{\circ}$ )	Lon ( $^{\circ}$ )	$\phi(^{\circ})$	$d\phi(^{\circ})$	$\delta t$	$d\delta t$	N
BL	AQDB	-20.48	-55.70	95.5	15.7	0.77	0.23	26
BL	BSCB	-21.00	-44.76	113.9	18.0	0.87	0.42	22
BL	C2SB	-18.77	-52.84	90.3	19.6	0.59	0.18	15
BL	CLDB	-10.87	-55.80	81.8	8.4	0.86	0.21	38
BL	CNLB	-29.31	-50.85	85.4	11.8	0.98	0.24	33
BL	ITAB	-27.23	-52.13	104.1	11.0	1.29	0.33	48
BL	ITQB	-29.66	-56.63	113.6	17.8	1.02	0.26	27
BL	ITRB	-19.70	-50.36	110.6	17.3	0.90	0.29	40
BL	PCMB	-21.61	-51.26	85.5	12.6	0.72	0.17	22
BL	PEXB	-12.11	-48.30	89.2	24.7	0.70	0.20	14
BL	PLTB	-31.76	-53.60	99.1	11.1	1.24	0.29	53
BL	PP1b	-17.60	-54.88	79.2	9.7	0.91	0.22	13
BL	PTGB	-24.72	-52.01	65.8	20.9	1.01	0.29	40
BL	TRCB	-22.79	-52.64	83.5	21.2	0.83	0.32	26
BR	ARAG	-15.71	-51.81	61.6	32.4	1.50	0.48	5
BR	BOAV	2.40	-60.52	71.5	8.8	0.79	0.18	4
BR	CZSB	-7.73	-72.70	129.0	0.0	1.23	0.00	1
BR	ETMB	-9.82	-66.21	45.5	34.6	1.08	0.07	2
BR	IPMB	-17.98	-48.21	85.0	16.6	0.69	0.24	23
BR	ITTB	-4.37	-55.73	106.4	30.8	0.78	0.45	13
BR	JANB	-15.06	-44.31	122.9	13.9	1.09	0.41	3
BR	MACA	-3.16	-60.68	119.6	17.4	0.62	0.14	13
BR	MALB	-1.85	-54.26	98.6	11.4	0.70	0.18	20
BR	MC01	-16.71	-43.94	105.0	0.0	0.31	0.00	1
BR	MCPB	-0.36	-52.06	93.4	18.3	0.98	0.37	15

Continued on next page

Table A.1 – continued from previous page

Net	Sta	Lat (°)	Lon (°)	$\phi(^{\circ})$	$d\phi(^{\circ})$	$\delta t$	$d\delta t$	N
BR	NPGB	-7.05	-55.36	84.7	10.3	0.90	0.36	15
BR	PDRB	-11.61	-56.73	111.8	12.7	1.01	0.30	17
BR	PRPB	-6.17	-49.81	76.6	16.0	1.11	0.26	15
BR	PTLB	-15.45	-59.14	91.3	26.7	0.82	0.20	24
BR	ROSB	-2.90	-44.12	88.4	12.9	1.09	0.22	20
BR	SALB	-15.90	-55.69	71.5	23.3	1.69	0.56	29
BR	SDBA	-12.41	-44.90	130.1	41.7	1.16	0.63	9
BR	SGCB	-0.12	-67.03	77.4	14.0	0.95	0.40	8
BR	SMTB	-8.86	-47.59	123.2	13.9	0.86	0.31	7
BR	SNDB	-11.97	-51.29	101.4	27.3	0.79	0.35	4
BR	TBTG	-4.19	-69.91	87.8	21.3	0.75	0.21	15
BR	TEFE	-3.51	-64.63	84.5	15.0	0.44	0.13	4
BR	TMAB	-2.37	-48.10	97.9	15.9	1.03	0.30	4
BR	VILB	-12.95	-60.20	116.9	37.1	0.79	0.24	13
XC	ALGR	-28.80	-53.03	87.4	16.5	0.98	0.32	9
XC	ANTJ	-22.00	-56.00	90.1	18.2	0.87	0.35	4
XC	AZCA	-28.08	-55.98	100.2	14.4	0.91	0.32	7
XC	BBLB	-18.67	-58.80	78.2	6.8	1.43	0.36	11
XC	BBRB	-18.28	-59.81	79.8	9.8	0.87	0.19	8
XC	BBSD	-17.19	-60.61	109.2	21.7	0.58	0.12	3
XC	BDQN	-20.45	-56.75	83.5	19.1	1.18	0.51	2
XC	CRSM	-27.49	-54.04	103.8	5.8	1.23	0.37	7
XC	DVLD	-16.64	-52.16	95.6	10.2	1.51	0.42	8
XC	ESFA	-24.96	-58.49	100.4	9.7	1.64	0.84	5
XC	FRBT	-25.98	-53.06	84.9	19.2	1.06	0.37	17
XC	MECA	-29.30	-58.17	100.5	3.8	0.95	0.33	4
XC	MURT	-21.66	-57.61	73.4	11.9	1.29	0.33	5
XC	NBRB	-14.32	-55.78	108.6	15.0	0.69	0.24	4
XC	PANT	-18.99	-56.62	71.0	0.0	1.85	0.00	1
XC	POCN	-16.62	-56.73	75.5	6.0	1.51	0.40	4
XC	PTET	-15.38	-57.16	93.4	8.1	0.92	0.39	5
XC	RODS	-30.35	-55.20	109.0	1.0	1.20	0.16	3
XC	RVDE	-19.03	-54.94	79.0	8.0	1.15	0.20	5
XC	TBOT	-31.68	-55.94	102.0	2.8	1.18	0.22	2
XC	UNIS	-29.07	-55.07	103.5	74.9	0.99	0.38	6
XC	VBST	-14.53	-60.02	108.0	30.1	0.92	0.47	10

## A.1 Figures

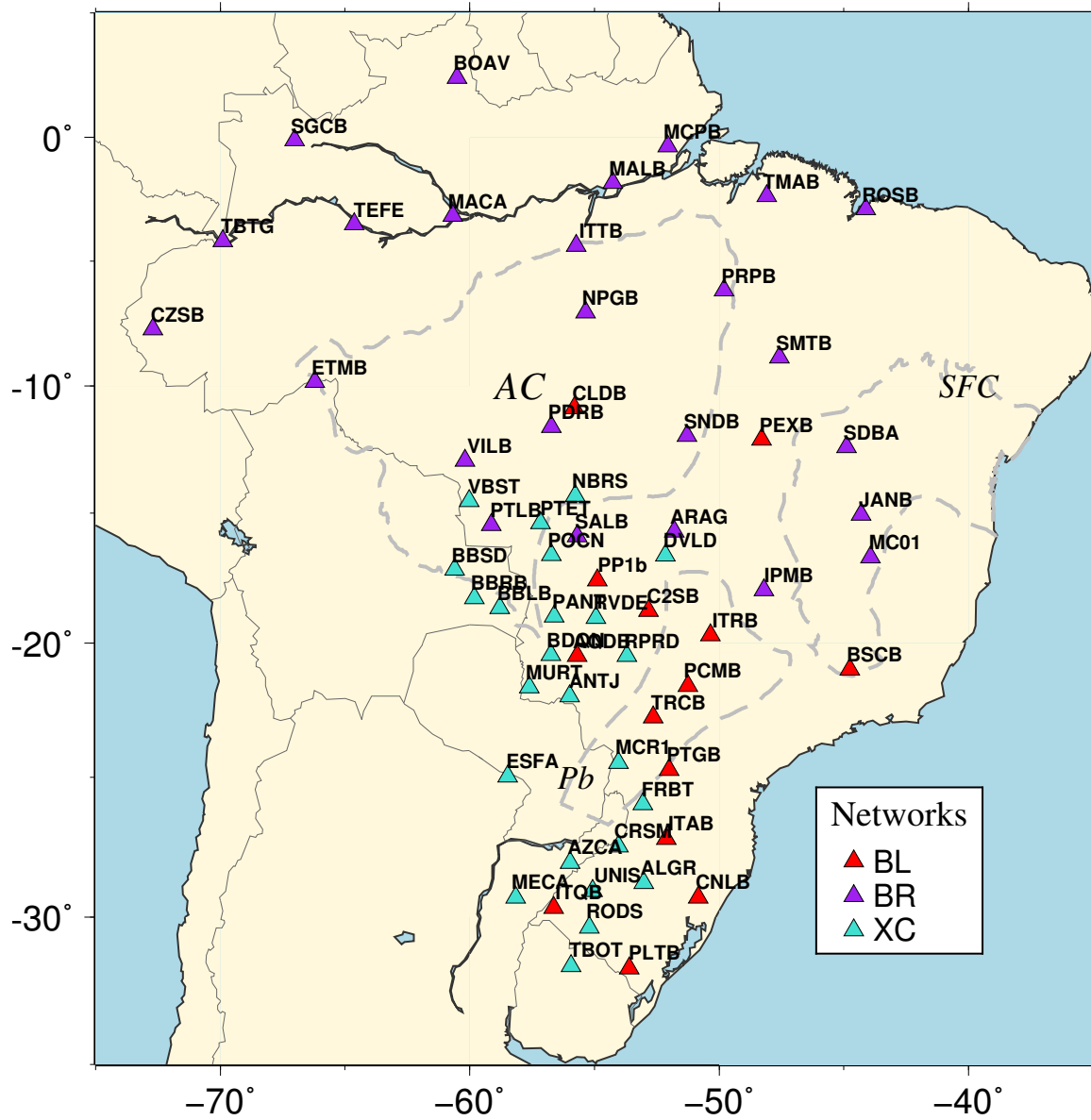


Figure A.1: Station names and their respective networks used in this paper. AC: Amazon craton; SFC: São Francisco craton; Pb: Paranapanema Block.